Kinematic instabilities in two-layer eccentric annular flows, part 2: shear-thinning and yield-stress effects

M. A. Moyers-Gonzalez · I. A. Frigaard

Abstract   This paper investigates the possibility of kinematic interfacial instabilities occurring during the industrial process of primary cementing of oil and gas wells. This process involves flows in narrow eccentric annuli that are modelled via a Hele-Shaw approach. The fluids present in primary cementing are strongly non-Newtonian, usually exhibiting shear-thinning behaviour and often with a yield stress. The study is a sequel to Moyers-González and Frigaard (J Eng Math, DOI 10.1007/s10665-007-9178-y, 2007), in which the base analysis has been developed for the case of two Newtonian fluids. The occurrence of static mud channels in primary cementing has been known of since the 1960s, (see McLean et al. 1966; SPE 1488), and is a major cause of process failure. This phenomenon is quantified, which provides a simple semi-analytic expression for the maximal volume of residual fluid left behind in the annulus, f_{static}, and illustrate the dependency of f_{static} on its five dimensionless parameters. It is shown that three of the four different types of static channel flows are linearly stable. Via dimensional analysis, it is shown that the base flows depend on a minimal set of eight dimensionless parameters and the stability problem depends on an additional two dimensionless parameters. This large dimensional parameter space precludes use of the full numerical solution to the stability problem as a predictive tool or for studying the various stability regimes. Instead a semi-analytical approach has been developed based on solution of the long-wavelength limit. This prediction of instability can be evaluated via simple quadrature from the base flow and is suitable for use in process optimisation.

Keywords   Hele-Shaw flow · Interfacial instability · Kinematic instability · Multi-layer flow stability · Primary cementing · Shear-thinning · Yield stress

M. A. Moyers-Gonzalez
Department of Mathematical Sciences, Durham University, South Road, Durham DH1 3LE, UK
e-mail: m.a.moyers-gonzalez@durham.ac.uk

I. A. Frigaard
Department of Mathematics, University of British Columbia, 2054-6250 Applied Science Lane, Vancouver, BC, Canada, V6T 1Z4

I. A. Frigaard (✉)
Department of Mechanical Engineering, University of British Columbia, 2054-6250 Applied Science Lane, Vancouver, BC, Canada, V6T 1Z4
e-mail: frigaard@mech.ubc.ca

1 Introduction

This paper investigates the possibility of kinematic interfacial instabilities occurring during the industrial process of primary cementing of oil and gas wells. This process involves displacement flows of multiple fluids in narrow eccentric annuli, see Fig. 1, with the eventual aim of placing a cement slurry in uncontaminated state within the well, between casing and formation where it may solidify to form a hydraulic seal. The process, its importance and some of the process problems that may occur are discussed in [1–3], as well as more widely in the technical literature.

Of relevance to us is a process of unsteady fingering that occurs when the displacement front advances faster along the wide side of the eccentric annulus than the narrow side, possibly leaving behind a channel of drilling mud on the narrow (lower) side of the annulus; see e.g. [4–6]. Since sections of oil and gas wells that are cemented tend to be very long, by comparison with their azimuthal length-scale, the process of unsteady fingering and channeling results in flow regimes that are pseudo-parallel with the axis of the well; see Fig. 1f. The onset of this type of unsteady fingering is predicted by the analysis in [7] which is based on a Hele-Shaw modeling approach developed in [8–10]. Although a Hele-Shaw approach is adopted, it is worth commenting that the occurrence of unsteady interfaces that lead to pseudo-parallel flows (Fig. 1f) is not controlled by local mobility ratios as in classical Hele-Shaw instabilities. Here there is a global imbalance caused by the annular eccentricity, i.e., fluids flow faster
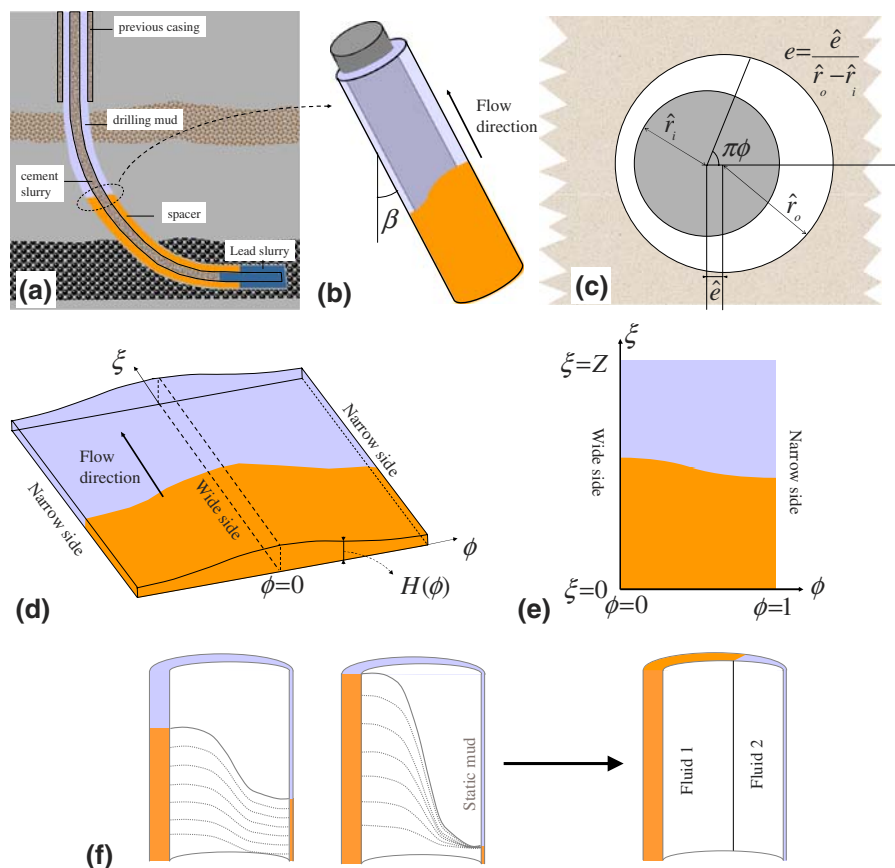

Fig. 1 Cementing geometries: **a** Schematic of fluid stages pumped during a primary cementing operation. **b** Uniform section of eccentric annulus. **c** Eccentric annular cross-section. **d** Periodic eccentric annular Hele-Shaw cell. **e** Final computational domain, assuming symmetry at wide and narrow sides of the annulus. **f** Unsteady and static mud channel displacements that evolve into parallel flows

in the wider part of the annulus, and also the annular flow rate is fixed, which constrains the local flow dynamics in a non-local fashion.

The aim of this paper is to study the stability of the parallel flows that evolve during displacements. Experimental evidence for such instabilities may be found in [11,12]. To study these flows, we consider perturbations about a parallel steady state, aligned in the direction of the annulus. The base flows are thus steady solutions of a steady Darcy-flow problem with two fluids. In such flows, in the absence of surface tension the interface is simply advected with the flow. Although instability can be studied using a steady Darcy model and with time evolution confined to the kinematic equation, this approach assumes that any interfacial instability grows initially on the advective timescale. This may, however, not be true when the instabilities are instigated by either viscosity or density differences, or perhaps by a forced temporal perturbation, e.g. pulsation of a pump, (this latter possibility is not studied here). Therefore, in [13,14] we have used a modified Hele-Shaw approach in which the linear acceleration terms are retained in the momentum balance. Evidently, should a linear instability grow then, eventually, the nonlinear inertial terms are also important. However, for predicting the onset of instability this approach suffices.

The study is a sequel to [15] (part 1) in which the base analysis has been developed for the case of two Newtonian fluids. The fluids present in primary cementing are, however, strongly non-Newtonian, usually exhibiting shear-thinning behaviour and often with a yield stress. This paper studies this practical reality, by extending the methodology of [15] to Herschel–Buckley fluids, which incorporate the simpler Bingham and power-law fluid models. For brevity we refer the reader to part 1 for a proper introduction to the industrial problem area and a motivation for our study.

In part 1 we showed that the Newtonian stability problem depended on six dimensionless parameters[1] and analysed this parametric dependency. Analytic solutions were developed for most of the limiting simplifications, e.g. concentric annuli, long-wavelength limits. With such a high-dimensional parameter space the results in [15] contain significant complexity. Some effects on stability, such as the effect of including a positive or negative density difference in an inclined annulus, were physically intuitive but not all.

Much of the complexity in the results arises from the competing effects of inertial accelerations and viscous dissipation. This is captured in the long wavelength analysis in [15], where the controlling parameter that switches from stable to unstable involves a product of the difference in interfacial velocities and a (weighted) difference in the Reynolds numbers, i.e., the kinematic viscosity difference. The interfacial velocities (capturing inertial effects) depend essentially on the viscosity difference. Thus, transitions between stable and unstable regimes show a strong dependency on the relative ratios of kinematic and dynamic viscosities, modulated by buoyancy. Part of the goal of the current paper is to see if the same overall picture is true once shear-thinning and yield-stress effects are included.

The physical expectations of including shear-thinning are unclear. In general shear-thinning will reduce the effective viscosity, but here we work with an imposed flow rate so that the effects on the mean velocity are less apparent and will depend on the effective viscosity ratio. This is further complicated by the fact that at the same imposed mean velocity, the shear rate will be higher and the viscosity consequently lower in a narrower part of the annulus for a fluid that shear-thins. Global effects on the stability of the multi-layer flow are therefore difficult to predict.

For yield-stress effects, to some extent physical intuition is easier. Increasing the yield stress will unequivocally increase the effective viscosity. However a new phenomenon arises, namely that of the fluids becoming "stuck" in the narrow annulus. This problematic phenomenon has been recognised in the cementing industry for at least 40 years, [4], and is a major cause of failure of primary cementing. In the context of our problem, we have multi-layer flows that contain a static unyielded channel, running axially along the well axis. Here we examine the effects of these channels on stability.

An outline of the paper and the chief results are as follows. Section 2 describes the extension of the model from part 1 to non-Newtonian fluids, and an analysis of the base flows. In particular in Sect. 2.2 we analyse the static mud-channel phenomenon, clarifying its dependency on dimensionless parameters and giving predictions of the maximal static residual annular volume. Section 3 presents the linear stability problem and reduces the dependency

---

[1] Note in [15] that one of the dimensionless densities is always unity.

of the problem to a minimal set of dimensionless numbers. A number of simplified analyses, leading to analytic and semi-analytical results are presented in Sect. 4. Section 5 presents numerical results, focusing in two subsections on shear-thinning and yield-stress effects. For the shear-thinning fluids for vertical annuli the results are ambiguous. For horizontal annuli the flow is stabilised by positive buoyancy and slightly destabilised by shear-thinning effects. The yield stress has the general effect of suppressing short wavelength instabilities. For sufficiently large yield-stress part of the annulus can become static. In cases where the static channel abuts the interface these flows are shown to be stable. We also show two new types of transition in our results: from stable to static channel and direct from unstable to static channel.

2 Non-Newtonian displacement flows

In this paper we shall consider the stability of base flows of two non-Newtonian fluids in a narrow eccentric annulus. The underlying Hele-Shaw model is derived in [13,14]; see also Fig. 1 for a schematic of the geometry. In [15] we have considered the simpler problem of stability of the parallel flow of two Newtonian fluids. Therefore, we keep our description minimalist to avoid undue repetition. As in part 1 we work in an unwrapped half-annular domain $\Omega : (\phi, \xi) \in [0, 1] \times [-\infty, \infty]$, which we assume is divided into two fluid domains, Ω_1 and Ω_2, by a smooth curve C that is defined by a level set function:

$$F(\phi, \xi, t) = 0. \tag{1}$$

The function $F(\phi, \xi, t)$ satisfies the gap-averaged kinematic equation:

$$\frac{H}{\epsilon} \frac{\partial F}{\partial t} - \frac{\partial \Psi}{\partial \xi} \frac{\partial F}{\partial \phi} + \frac{\partial \Psi}{\partial \phi} \frac{\partial F}{\partial \xi} = 0, \tag{2}$$

where $H(\phi) = 1 + e \cos \pi \phi$ denotes the gap width, ϵ is the ratio of advective and viscous timescales, and $\Psi(\phi, \xi, t)$ is the gap-averaged stream function. The annular eccentricity is e and the annulus is inclined at angle β to the vertical: see Fig. 1b and c. In general all variables we use will be dimensionless. When dimensional variables are defined they will be denoted with a $\hat{}$ symbol.

The physical properties of each fluid are assumed constant in each domain, and the stream-function formulation of the Darcy-like equations gives us that

$$\rho_k \nabla \cdot \left[\frac{\nabla \Psi_t}{H} \right] + \nabla \cdot \mathbf{S}_k = 0, \quad (\phi, \xi) \in \Omega_k, k = 1, 2, \tag{3}$$

in each fluid domain. The vectorfield $\mathbf{S}_k$ contains the components of modified pressure gradient in fluid k. As the Hele-Shaw approach is taken, the modified pressure gradient is related to the mean velocity by an hydraulic relation that can be calculated locally by considering the flow of the fluid between parallel plates; see e.g. [8]. In general, $\mathbf{S}_k$ will have form:

$$\mathbf{S}_k = \left(\frac{\chi_k(|\nabla \Psi|) + \tau_{k,Y}/H}{|\nabla \Psi|} \right) \nabla \Psi \Leftrightarrow |\mathbf{S}_k| > \tau_{k,Y}/H, \tag{4}$$

$$|\nabla \Psi| = 0 \Leftrightarrow |\mathbf{S}_k| \leq \tau_{k,Y}/H. \tag{5}$$

Here $\tau_{k,Y}$ denotes the yield stress of fluid k. We assume that our fluids are shear-thinning yield-stress fluids, modeled for simplicity by the Herschel–Bulkley model, each characterised by $\tau_{k,Y}$, a dimensionless consistency κ_k and a power-law index n_k. The function χ is a positive increasing function of $|\nabla \Psi|$, which represents the purely viscous part of the frictional pressure gradient. The exact form of χ_k depends on H, and on the rheological parameters that characterise the fluid. For the Herschel–Bulkley model, χ is defined implicitly by the relation:

$$|\nabla \Psi| = \begin{cases} 0 & \chi_k \leq 0, \\ \dfrac{H^{m_k+2}}{\kappa_k^{m_k(m_k+2)}} \dfrac{\chi_k^{m_k+1}}{(\chi_k + \tau_{k,Y}/H)^2} \left[\chi_k + \dfrac{(m_k + 2)\tau_{k,Y}}{(m_k + 1)H} \right] & \chi_k > 0, \end{cases} \tag{6}$$

where $m_k = 1/n_k$.

To give a brief physical explanation of the above model (2–6), first note that the gap-averaged velocity field in directions (ϕ, ξ) is simply $(-\Psi_\xi, \Psi_\phi)/H$, and so (2) simply says that the interface is advected with the mean flow. In deriving (3) the usual Hele-Shaw steps have been followed except that we have chosen to work with the viscous timescale instead of the advective timescale. Typically one assumes the process is steady and discards all the inertial terms with the argument that the Reynolds number times the aspect ratio (gap/length) of the duct is small. As discussed in the Introduction, here we look for instabilities that may arise from a combination of density and viscosity differences, or (later) from flow oscillation. In these cases it is not clear that the only timescale is the advective timescale and hence we have retained also the time derivatives. If instabilities grow then of course neglect of the nonlinear inertial terms is questionable, but for now the objective is to predict onset. The other difference with some Hele-Shaw treatments is that we have chosen to work with the stream-function formulation rather than the pressure formulation. This is because for yield-stress fluids the pressure gradient is indeterminate in unyielded flow regions. To return to something familiar for the reader, if we set $\tau_Y = 0$, then (6) becomes explicit:

$$\chi_k = \kappa_k \left[\frac{(m_k + 2)|\nabla \Psi|}{H^{m_k+2}} \right]^{1/m_k},$$

which leads to the familiar linear relation for $m_k = 1$, (i.e., for Newtonian fluids; see part 1), and on neglecting the time derivatives in (3) we have a linear elliptic equation familiar from 2D porous media flows.

Equation 3 is supplemented with the following two boundary conditions:

$$\Psi(0, \xi, t) = 0. \tag{7}$$

$$\Psi(1, \xi, t) = 1, \tag{8}$$

on the wide ($\phi = 0$) and narrow ($\phi = 1$) sides of the annulus, respectively. The physical interpretation is simply that the flow rate through the annulus is fixed, with $\Psi(1, \xi, t) = 1$ in (8) arising from the scaling of the velocity with the mean velocity. At the interface between fluids the following two jump/continuity conditions are satisfied,

$$\Psi|_1^2 = 0, \tag{9}$$

$$\left[\left(\frac{\rho_k \cos \beta}{St^*}, \frac{\rho_k \sin \beta \sin \pi \phi}{St^*} \right) + \frac{\rho_k}{H} \nabla \Psi_t + \mathbf{S}_k \right] \cdot \nabla F|_1^2 = 0. \tag{10}$$

The first of these is simply continuity of Ψ, i.e., of the normal velocity, whereas (10) defines the jump in normal derivative of Ψ. Condition (10) comes from continuity of the pressure; see [13,15] for further explanation.

For a given interface, we observe that these unsteady displacement flows are characterised by 11 dimensionless parameters. These parameters are: two dynamic parameters, ϵ and St^*; two geometric parameters, e and β; four dimensionless physical parameters for each fluid, $\rho_k, \kappa_k, \tau_{k,Y}, n_k, k = 1, 2$; but note that one of the densities is unity as we have scaled density with the maximum density. Although complex, we shall see later that there is some redundancy in the parameter space, when considering specific aspects of the flow. We shall discuss the dimensionless parameters in more detail in Sect. 3.2.

2.1 Base two-layer flows

We study the stability of steady multi-layer flows, that arise as one fluid fingers past another during an annular displacement at unit flow rate. These steady base flows satisfy (2–10) and are parallel to the ξ-axis, hence $\Psi = \Psi(\phi)$. We assume that the annulus is occupied by two fluids: fluid 1 occupying $\phi \in [0, \phi_i)$ and fluid 2 occupying $\phi \in (\phi_i, 1]$. The interface level set is thus $F = \phi - \phi_i$. Our solutions are steady parallel solutions of (3), which implies $\mathbf{S}_k = (S_{k,\phi}, S_{k,\xi}) = (S_{k,\phi}, 0)$, and

$$\frac{\partial}{\partial \phi} S_{k,\phi} = 0. \tag{11}$$

Since we also have:

$$S_{k,\phi} = -\frac{\partial p}{\partial z} - \frac{\rho_k \cos \beta}{St^*}, \tag{12}$$

with (10) this implies that the axial pressure gradient is continuous at the interface. Therefore the fluid layers are acted on by a constant pressure gradient, modified by an axial hydrostatic pressure that is different in each fluid layer, due to the density jump. Since $S_{k,\phi}$ is independent of ϕ and ξ, (by definition, we look for solutions independent of ξ), we write:

$$S_{1,\phi} = A, \qquad S_{2,\phi} = A - b, \tag{13}$$

where b is a buoyancy parameter, given by:

$$b = \frac{\rho_2 - \rho_1}{St^*} \cos \beta. \tag{14}$$

Typically, in a cementing scenario where fingering occurs, b is negative: the heavier cement channels past the more viscous drilling mud that is left behind on the narrow side. The constant A represents the modified pressure gradient in the axial direction, within fluid 1, and must be found as part of the base solution. In order to find A we use (8):

$$1 = \Psi(1) = \int_0^{\phi_i} \left. \frac{\partial \Psi}{\partial \phi} \right|_{k=1} d\phi + \int_{\phi_i}^1 \left. \frac{\partial \Psi}{\partial \phi} \right|_{k=2} d\phi. \tag{15}$$

where,

$$\left. \frac{\partial \Psi}{\partial \phi} \right|_{k=1} = \Upsilon \left(\frac{A}{\kappa_1}, \frac{\tau_{1,Y}}{\kappa_1}, H, m_1 \right), \tag{16}$$

$$\left. \frac{\partial \Psi}{\partial \phi} \right|_{k=2} = \Upsilon \left(\frac{A-b}{\kappa_2}, \frac{\tau_{2,Y}}{\kappa_2}, H, m_2 \right), \tag{17}$$

$$\Upsilon(w, x, y, z) = \begin{cases} 0, & |w|y \le x, \\ \mathrm{sgn}(w) \dfrac{y^2(|w|y - x)^{z+1}}{|w|y(z+2)} \left(1 + \dfrac{x}{|w|y(z+1)} \right), & \\ & |w|y > x, \end{cases} \tag{18}$$

c.f. Eq. 6. Note that ϕ-dependency enters through $H(\phi)$.

Equation 15 can be interpreted as a nonlinear equation for A/κ_1. It is straightforward to show that the function $\Upsilon(w, x, y, z)$ increases monotonically with w, and from this we find that (15) has a unique solution $A/\kappa_1 = A(\phi_i)/\kappa_1$. Once $A(\phi_i)/\kappa_1$ is determined, the base solution can be computed via integration. More precisely, we have that the base solution will depend parametrically on ϕ_i, e, κ_1/κ_2, b/κ_2, $\tau_{1,Y}/\kappa_1$, m_1, $\tau_{2,Y}/\kappa_2$, m_2. By comparison with part 1, where we considered Newtonian fluids, $m_k = 1$, we see that we have four additional dimensionless parameters to consider, i.e., $\tau_{1,Y}/\kappa_1$, m_1, $\tau_{2,Y}/\kappa_2$, m_2. The ratios $\tau_{k,Y}/\kappa_k$ will be denoted B_k, and are the Bingham numbers for each fluid, which represent the balance of yield and viscous stresses.

Some examples of base solution are shown below in Fig. 2. In Fig. 2a we have no buoyancy force; $\Psi(\phi)$ increases from 0 to 1 with ϕ, but there is a discontinuity in the gradient at the interface, $\phi = \phi_i$. Recall that the derivative of $\Psi(\phi)$ divided by $H(\phi)$ gives the axial velocity. In a Hele-Shaw cell, at an interface between fluids, only the pressure and normal velocity are conserved, i.e., a jump in the tangential velocity is permitted. Figure 2b shows a base solution for which fluid 2 is static in a region close to $\phi = 1$ and Fig. 2c shows a base flow for which the entire layer of fluid 2 is static. This phenomena results from the yield stress in fluid 2 being too large. In the context of the industrial displacement flow, this would correspond to the drilling mud being left behind in a static channel on the narrow side of the annulus, which is detrimental to the process effectiveness. We study these static channels in the section immediately below. Finally, Fig. 2d illustrates that with significant buoyancy, the base flow velocity can be in the negative direction, i.e., the flow can be counter-current.
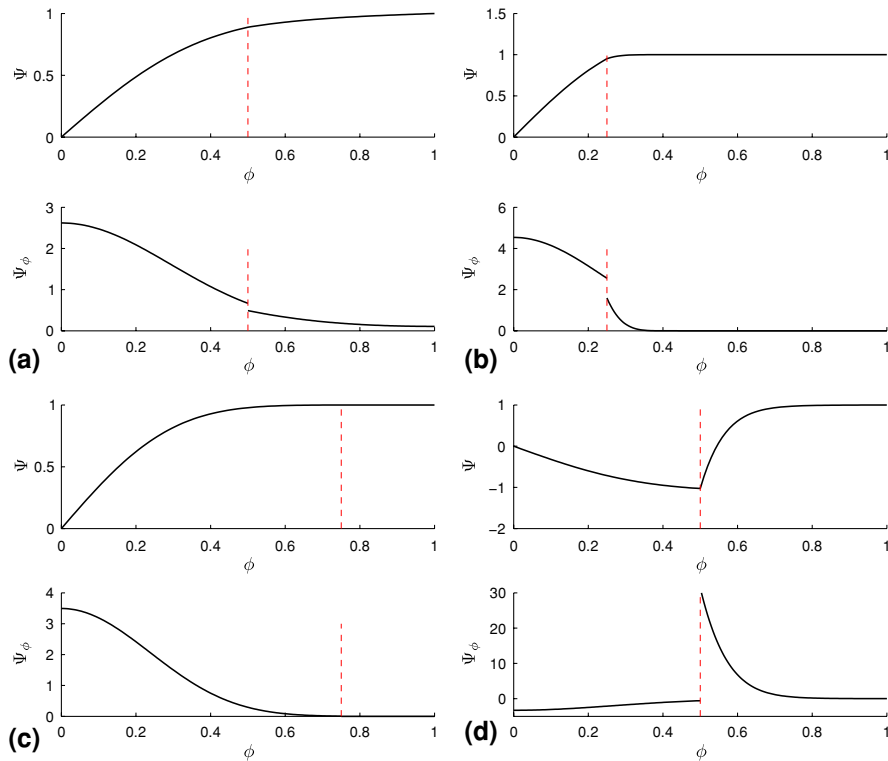
Fig. 2 Example base solutions: **a** $\phi_i = 0.5$, $e = 0.3$, $\kappa_1/\kappa_2 = 1$, $b/\kappa_2 = 0$, $B_1 = 1$, $m_1 = 2$, $B_2 = 1$, $m_2 = 1$. **b** $\phi_i = 0.25$, $e = 0.75$, $\kappa_1/\kappa_2 = 2$, $b/\kappa_2 = -1.25$, $B_1 = 0.25$, $m_1 = 2$, $B_2 = 5$, $m_2 = 5$. **c** $\phi_i = 0.75$, $e = 0.75$, $\kappa_1/\kappa_2 = 2$, $b/\kappa_2 = -1.25$, $B_1 = 0.25$, $m_1 = 2$, $B_2 = 5$, $m_2 = 5$. **d** $\phi_i = 0.5$, $e = 0.5$, $\kappa_1/\kappa_2 = 0.5$, $b/\kappa_2 = -5$, $B_1 = 0.25$, $m_1 = 2$, $B_2 = 1$, $m_2 = 5$. Interface position is marked by the *vertical broken line*

2.2 Static fluid layers

We have seen in Fig. 2b and c that it is possible for fluid 2 to be stationary, in all or part of $(\phi_i, 1]$. It is also possible for all or part of the fluid 1 layer to be static. In the context of flow stability, we shall later see that certain of these base flows are linearly stable and therefore it is of interest to define where these flows can be found. From the practical perspective, it is however the fluid 2 static layers that are of interest.

Physically, a static channel occurs when the modified pressure gradient is not large enough to overcome the yield stress of the fluid. Since the modified pressure gradient is constant in each fluid layer and since $H(\phi)$ decreases, yield-stress fluids become static at the largest values of ϕ in each layer. For the mud, fluid 2, the minimal annular gap is at $\phi = 1$, where $H = 1 - e$, and so there can only be a static "mud" channel in fluid 2 if

$$|A(\phi_i) - b| < \frac{\tau_{2,Y}}{1 - e}. \tag{19}$$

If (19) is satisfied, the entire layer will be static if

$$|A(\phi_i) - b| < \frac{\tau_{2,Y}}{H(\phi_i)}, \tag{20}$$

and otherwise $[\phi_s, 1] \subset (\phi_i, 1]$ is static, where $|A(\phi_i) - b| = \tau_{2,Y}/H(\phi_s)$. The fully static channels are of industrial relevance, since they represent the residual mud that may possibly remain in the wellbore after cementing. Suppose now that (20) is satisfied for some ϕ_i. We ask what is the maximal azimuthal width of fully static mud channel that can exist?

First of all, if the mud is static, then the modified pressure gradient is determined wholly from the fluid 1 layer, via:

$$1 = \int_0^{\phi_i} \left. \frac{\partial \Psi}{\partial \phi} \right|_{k=1} \mathrm{d}\phi. \tag{21}$$

From our previous discussion, we see that the modified pressure gradient $A(\phi_i)/\kappa_1$ will depend on ϕ_i, e, $\tau_{1,Y}/\kappa_1$ and m_1. Evidently as $\phi_i \to 0$, if the mud remains static, then $A(\phi_i)/\kappa_1 \to \infty$ since the unit flow rate is forced through an increasingly narrow azimuthal gap. It follows that for some ϕ_i, there will be a value of $A(\phi_i)$ for which:

$$|A(\phi_i) - b| = \frac{\tau_{2,Y}}{H(\phi_i)}, \tag{22}$$

which defines the smallest interface position for which the mud layer remains fully static. We denote this interface position by $\phi_i = \phi_{i,\min}$, and the maximal azimuthal width of mud channel is therefore $1 - \phi_{i,\min}$. Dividing through by κ_1, we see that $\phi_{i,\min}$ depends parametrically on: e, B_1, m_1, b/κ_1 and $\tau_{2,Y}/\kappa_1$. More useful practically is to know the maximal volume of the annulus occupied by static mud, say f_{static}:

$$f_{\text{static}} = \int_{\phi_{i,min}}^1 H(\phi) \, \mathrm{d}\phi = 1 - \phi_{i,\min} - \frac{e}{\pi} \sin \pi \phi_{i,\min}.$$

Note that f_{static} is effectively a volume fraction, $f_{\text{static}} \in (0, 1)$. In Figs. 3 and 4 we explore some of this parametric variation.

In general we see that the maximal residual mud fraction, f_{static}, increases with the ratio $\tau_{2,Y}/\kappa_1$ and decreases with B_1 and with n_1. The former is a simple increase in the stress level required to mobilise fluid 2, and therefore is wholly intuitive. The decrease with B_1 and with n_1 is also unsurprising, as these increase the viscous stress generated in fluid 1, which is transmitted to fluid 2 via the axial pressure gradient. Usually we find that f_{static} increases with the eccentricity e, and it is only at low n_1 that some non-monotone behaviour is found. The precise reasons for the non-monotone behaviour are unclear. Finally, comparing Figs. 3 and 4 directly, we see that reducing b has the effect of decreasing f_{static}. In summary, most of these effects are physically intuitive.

A similar analysis can be carried out for the possibility of fluid 1 static layers. The only difference to note is that if fluid 1 is static anywhere in the fluid layer, it is static at the interface which is the narrowest part of the annulus occupied by fluid 1.

3 Stability of parallel two-layer flows

As in part 1, [15], we consider linear perturbation of the base flows from Sect. 2.1, which we denote by $\Psi_k = \Psi_{k,0}(\phi)$ and $\mathbf{S}_k = (S_{k,\phi,0}, 0)$, $k = 1, 2$, with interface position $\phi_i = \phi_{i,0}$. We linearise, assume normal mode expansions and transform to an eigenvalue problem, in the usual way. More formally, for $\delta \ll 1$ we assume the expansions:

$$\Psi_k = \Psi_{k,0} + \delta \Psi_{k,1} + \delta^2 \Psi_{k,2} + ...,$$
$$\mathbf{S}_k = (S_{k,\phi,0}, 0) + \delta \mathbf{S}_{k,1} + \delta^2 \mathbf{S}_{k,2} + ...$$
$$\phi_i = \phi_{i,0} + \delta h + ...,$$

insert into (2–10), expand in powers of δ.

$$\nabla \Psi_k = (\Psi_{k,0,\phi} + \delta \Psi_{k,1,\phi} + ..., \delta \Psi_{k,1,\xi} + ...) \tag{23}$$

$$|\nabla \Psi| = [(\Psi_{k,0,\phi} + \delta \Psi_{k,1,\phi} + ...)^2 + (\delta \Psi_{k,1,\xi} + ...)^2]^{\frac{1}{2}}$$
$$\sim |\Psi_{k,0,\phi}| + \delta \mathrm{sgn}(\Psi_{k,0,\phi}) \Psi_{k,1,\phi} + O(\delta^2). \tag{24}$$
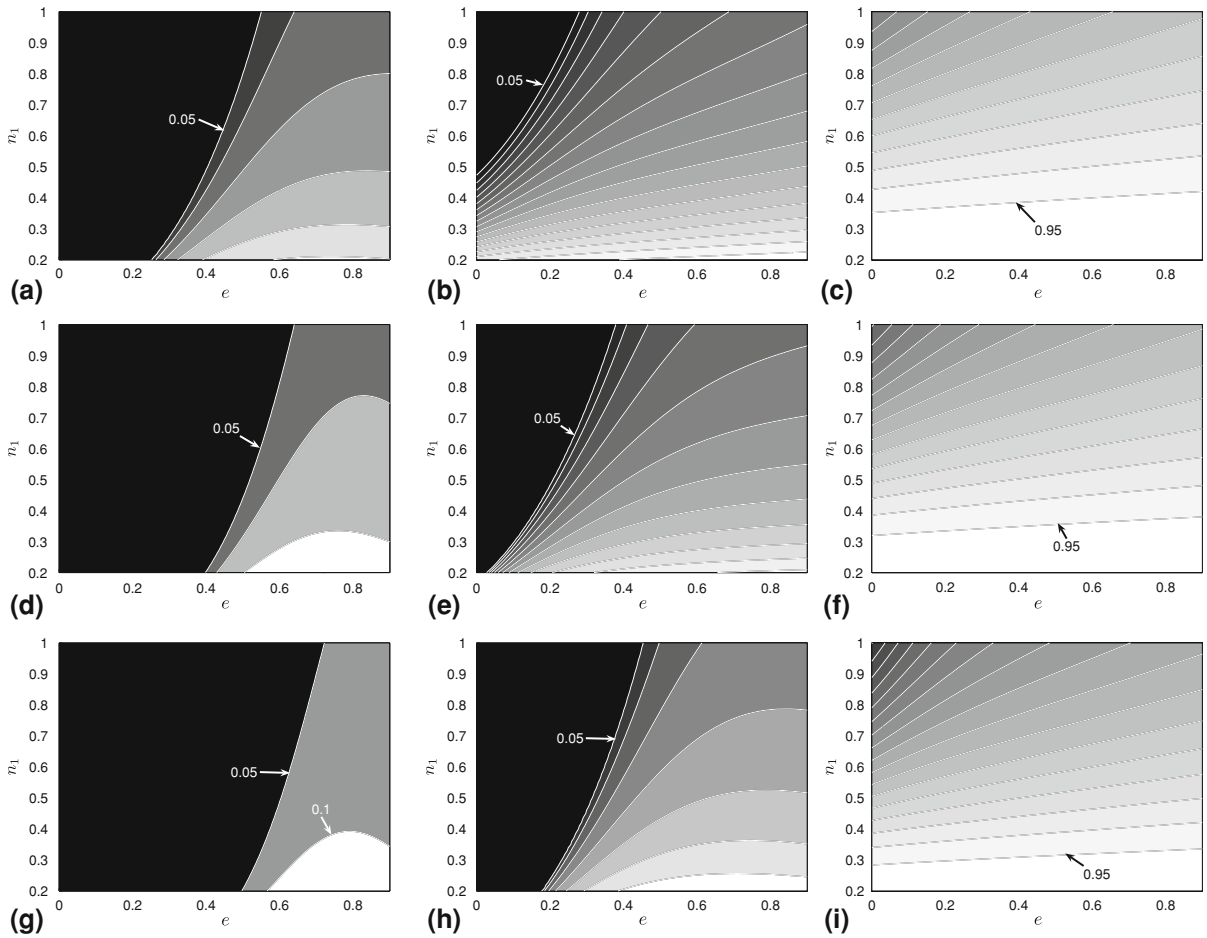
Fig. 3 Variations in maximal displaced fluid volume left static in the annulus, f_{static} with $b = 0$. **a** $B_1 = 0$, $\tau_{2,Y}/\kappa_1 = 1$. **b** $B_1 = 0$, $\tau_{2,Y}/\kappa_1 = 2$. **c** $B_1 = 0$, $\tau_{2,Y}/\kappa_1 = 5$. **d** $B_1 = 0.5$, $\tau_{2,Y}/\kappa_1 = 1$. **e** $B_1 = 0.5$, $\tau_{2,Y}/\kappa_1 = 2$. **f** $B_1 = 0.5$, $\tau_{2,Y}/\kappa_1 = 5$. **g** $B_1 = 1$, $\tau_{2,Y}/\kappa_1 = 1$. **h** $B_1 = 1$, $\tau_{2,Y}/\kappa_1 = 2$. **i** $B_1 = 1$, $\tau_{2,Y}/\kappa_1 = 5$. *Shaded contours* are spaced at intervals of $\Delta f_{\text{static}} = 0.05$

When the fluid is yielded we find:

$$\mathbf{S}_{k,1} = \left[\chi_k'(|\Psi_{k,0,\phi}|)\Psi_{k,1,\phi}, \; \left(\chi_k(|\Psi_{k,0,\phi}|) + \frac{\tau_{k,Y}}{H}\right)\frac{\Psi_{k,1,\xi}}{|\Psi_{k,0,\phi}|} \right], \tag{25}$$

but otherwise $\mathbf{S}_k$ is indeterminate. The linearised equation for Ψ_1 is

$$\nabla \cdot \left[\mathbf{S}_{k,1} + \frac{\rho_k}{H}\nabla\Psi_{k,1,,t} \right] = 0, \quad \text{in } \Omega_k. \tag{26}$$

The kinematic equation and boundary conditions are:

$$\frac{H}{\epsilon}h_t + \Psi_{k,1,\xi} + \Psi_{k,0,\phi}h_\xi = 0, \quad \text{at } \phi = \phi_{i,0} \tag{27}$$

$$\Psi_{1,1}(0, \xi, t) = 0, \tag{28}$$

$$\Psi_{2,1}(1, \xi, t) = 0, \tag{29}$$

The jump conditions (9) and (10) are linearised, first about the basic flow and secondly onto the basic flow interface position. Thus, at $O(\delta)$, condition (9) becomes

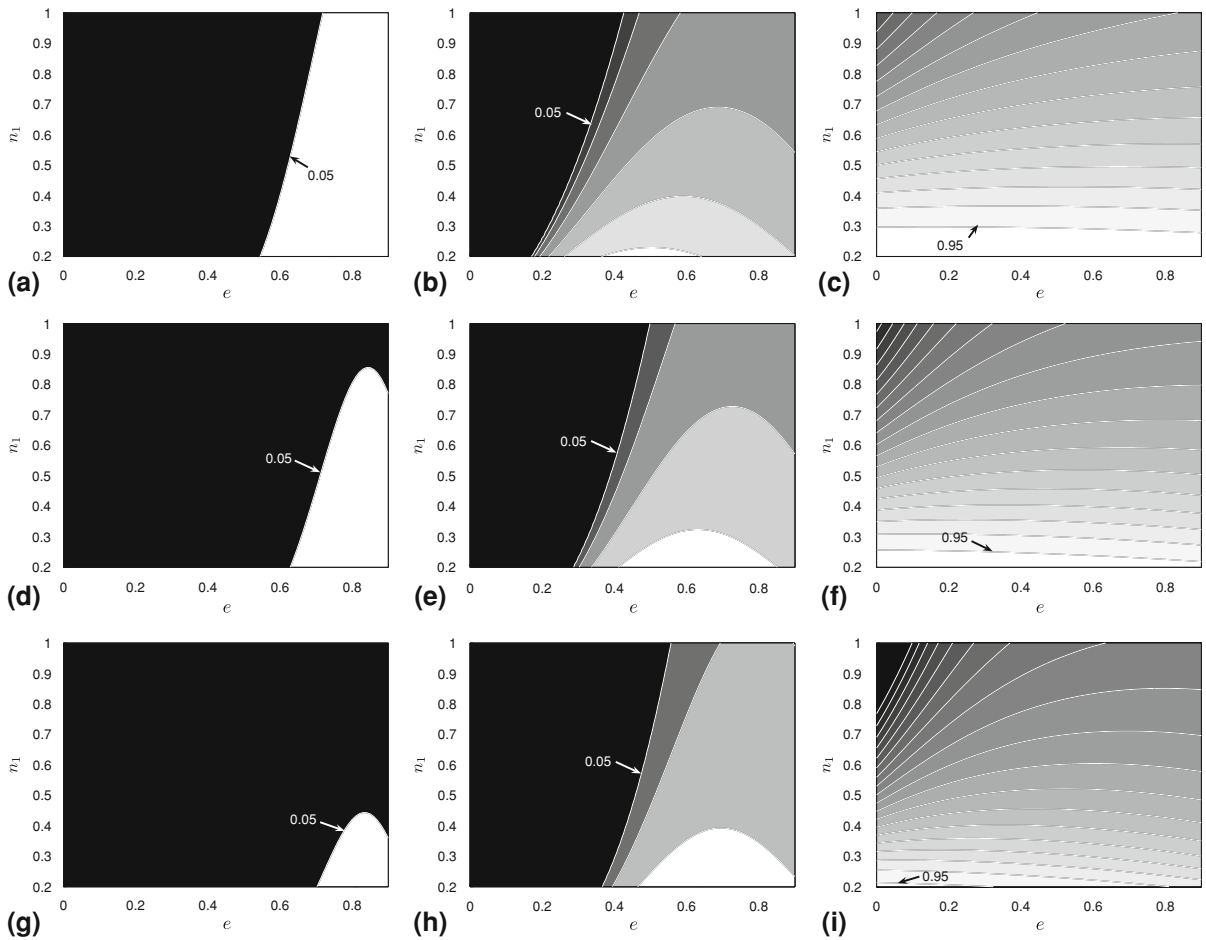$$(\Psi_{k,1} + h\Psi_{k,0,\phi})\big|_{k=1}^{k=2} = 0, \qquad \text{at } \phi = \phi_{i,0}, \tag{30}$$

Fig. 4 Variations in maximal displaced fluid volume left static in the annulus, f_{static} with $b = -1$. **a** $B_1 = 0$, $\tau_{2,Y}/\kappa_1 = 1$. **b** $B_1 = 0$, $\tau_{2,Y}/\kappa_1 = 2$. **c** $B_1 = 0$, $\tau_{2,Y}/\kappa_1 = 5$. **d** $B_1 = 0.5$, $\tau_{2,Y}/\kappa_1 = 1$. **e** $B_1 = 0.5$, $\tau_{2,Y}/\kappa_1 = 2$. **f** $B_1 = 0.5$, $\tau_{2,Y}/\kappa_1 = 5$. **g** $B_1 = 1$, $\tau_{2,Y}/\kappa_1 = 1$. **h** $B_1 = 1$, $\tau_{2,Y}/\kappa_1 = 2$. **i** $B_1 = 1$, $\tau_{2,Y}/\kappa_1 = 5$. *Shaded contours* are spaced at intervals of $\Delta f_{\text{static}} = 0.05$

and we note that it is the derivative of this quantity with respect to ξ that appears in (27), i.e., it is irrelevant which fluid is considered for the kinematic condition. Expanding $(\mathbf{S}_k + (\rho_k/H)\nabla\Psi_{k,t}) \cdot \mathbf{n}$, about $\phi = \phi_{i,0}$ we have:

$$\left[\mathbf{S}_k + \frac{\rho_k}{H}\nabla\Psi_{k,t}\right] \cdot \mathbf{n} \sim S_{k,0,\phi} + \delta h \frac{\partial}{\partial\phi} S_{k,0,\phi} + \delta S_{k,1,\phi} + \frac{\rho_k}{H}[\Psi_{k,0,\phi t} + \delta h\Psi_{k,0,\phi\phi t} + \delta\Psi_{k,1,\phi t}] \quad \text{at } \phi = \phi_{i,0}$$

$$(1, \tan\beta \sin\pi\phi_i) \cdot \mathbf{n} \sim 1 - \delta h_\xi \tan\beta \sin\pi\phi_{i,0}$$

Noting that $S_{k,0,\phi}$ is independent of ϕ and $\Psi_{k,0}$ independent of t, at $O(\delta)$, condition (10) becomes

$$\left(S_{k,1,\phi} + \frac{\rho_k}{H}\Psi_{k,1,\phi t}\right)\Big|_{k=1}^{k=2} = bh_\xi \tan\beta \sin\pi\phi_{i,0}, \quad \text{at } \phi = \phi_{i,0}, \tag{31}$$

We now assume a normal-mode expansion of the linear perturbation, with modes of form:

$$\Psi_{1,k} \sim f_k(\phi)e^{i(\alpha\xi - st)}, \qquad h \sim h_0 e^{i(\alpha\xi - st)},$$

which we substitute in (26–31) to give:

$$0 = D[\chi_1'(|\Psi_{1,0,\phi}|)Df_1] - \alpha^2 \left[\frac{\chi_1(|\Psi_{1,0,\phi}|) + \dfrac{\tau_{1,Y}}{H}}{|\Psi_{1,0,\phi}|} \right] f_1,$$

$$-\mathrm{i}s\rho_1 \left(D\left(\frac{D}{H}\right) - \frac{\alpha^2}{H} \right) f_1, \quad \phi \in (0, \phi_{i,0}), \tag{32}$$

$$0 = D[\chi_2'(|\Psi_{2,0,\phi}|)Df_2] - \alpha^2 \left[\frac{\chi_2(|\Psi_{2,0,\phi}|) + \dfrac{\tau_{2,Y}}{H}}{|\Psi_{2,0,\phi}|} \right] f_2,$$

$$-\mathrm{i}s\rho_2 \left(D\left(\frac{D}{H}\right) - \frac{\alpha^2}{H} \right) f_2, \quad \phi \in (\phi_{i,0}, 1), \tag{33}$$

$$f_1(0) = 0, \tag{34}$$

$$f_2(1) = 0, \tag{35}$$

and at $\phi = \phi_{i,0}$:

$$-\frac{H}{\epsilon}sh_0 + \alpha(f_k + \Psi_{k,0,\phi}h_0) = 0, \tag{36}$$

$$(h_0\Psi_{0,k,\phi} + f_k)|_1^2 = 0, \tag{37}$$

$$\left[(\chi_k'(|\Psi_{0,k,\phi}|) - \mathrm{i}s\frac{\rho_k}{H})Df_k \right]\Big|_{k=1}^{k=2} = \mathrm{i}\alpha b h_0 \tan\beta \sin\pi\phi_{i,0}. \tag{38}$$

Assuming for the moment that both fluid layers are fully mobile, linear stability of this flow is governed by the system (32–38), which is an an eigenvalue problem for $s = s_R + \mathrm{i}s_I \in \mathbb{C}$. Linear instability is found if for any $\alpha \in \mathbb{R}$ we have an eigenvalue with $s_I > 0$. We may observe that, including specification of α and $\phi_{i,0}$, this eigenvalue problem for s depends upon 13 dimensionless parameters.

3.1 Reduction to a minimal set of dimensionless parameters

We are able to simplify the stability problem by dividing through (32) by κ_1, (33) by κ_2 and (38) by κ_2. With the following definitions:

$$B_1 = \frac{\tau_{1,Y}}{\kappa_1}, \qquad B_2 = \frac{\tau_{2,Y}}{\kappa_2}, \tag{39}$$

$$Re_1 = \frac{\epsilon\rho_1}{\kappa_1}, \qquad Re_2 = \frac{\epsilon\rho_2}{\kappa_2}, \tag{40}$$

$$\varphi_\kappa = \frac{\kappa_1}{\kappa_2} \qquad \varphi_b = \frac{b}{\kappa_2} \tag{41}$$

$$\lambda = \frac{s}{\epsilon}, \tag{42}$$

eigenvalues $\lambda \in \mathbb{C}$ are found from the solution to:

$$0 = D\left[\frac{\chi_1'(|\Psi_{1,0,\phi}|)}{\kappa_1}Df_1 \right] - \alpha^2 \left[\frac{|A/\kappa_1|}{|\Psi_{1,0,\phi}|} \right] f_1, -\mathrm{i}\lambda Re_1 \left(D\left(\frac{D}{H}\right) - \frac{\alpha^2}{H} \right) f_1, \quad \phi \in (0, \phi_{i,0}), \tag{43}$$

$$0 = D\left[\frac{\chi_2'(|\Psi_{1,0,\phi}|)}{\kappa_2}Df_2 \right] - \alpha^2 \left[\frac{|\varphi_\kappa A/\kappa_1 - \varphi_b|}{|\Psi_{2,0,\phi}|} \right] f_2, -\mathrm{i}\lambda Re_2 \left(D\left(\frac{D}{H}\right) - \frac{\alpha^2}{H} \right) f_2, \quad \phi \in (\phi_{i,0}, 1), \tag{44}$$

$$f_1(0) = 0, \tag{45}$$

$$f_2(1) = 0, \tag{46}$$

and at $\phi = \phi_{i,0}$:

$$-H\lambda h_0 + \alpha(f_k + \Psi_{k,0,\phi}h_0) = 0, \tag{47}$$

$$(h_0\Psi_{0,k,\phi} + f_k)|_1^2 = 0, \tag{48}$$

$$\left[\frac{\chi_2'(|\Psi_{1,0,\phi}|)}{\kappa_2} - \mathrm{i}\frac{\lambda\mathrm{Re}_2}{H}\right]Df_2 = \varphi_\kappa\left[\frac{\chi_1'(|\Psi_{1,0,\phi}|)}{\kappa_1} - \mathrm{i}\frac{\lambda\mathrm{Re}_1}{H}\right]Df_1 + \mathrm{i}\alpha\varphi_b h_0 \tan\beta\sin\pi\phi_{i,0}, \tag{49}$$

Recall that the base solution $\Psi_{k,0}$ is fully determined by the eight parameters: $\phi_{i,0}, e, \varphi_\kappa, \varphi_b, \mathrm{B}_1, m_1, \mathrm{B}_2, m_2$, which also determine A/κ_1 above. Note also from the base solution that:

$$|A| = \chi_1(|\Psi_{1,0,\phi}|) + \frac{\tau_{1,Y}}{H}, \quad |A-b| = \chi_2(|\Psi_{2,0,\phi}|) + \frac{\tau_{2,Y}}{H}.$$

We must add to this set of eight parameters the two reduced Reynolds numbers, Re_1 and Re_2. Note that, although one of the dimensionless densities is unity, due to the scaling, the two reduced Reynolds numbers are independent since ϵ is also included in these. Finally, we may note from (6) that $\chi_k'(|\Psi_{k,0,\phi}|)$ is defined via implicit differentiation of (6):

$$\chi_k' = \frac{\kappa_k^{m_k}(m_k+2)}{H^{m_k+2}\chi_k^{m_k}}\left[\frac{(\chi_k + \tau_{k,Y}/H)^3}{m\chi_k^2 + \dfrac{m_k(m_k+2)\chi_k\tau_{k,Y}}{(m_k+1)H} + \dfrac{\tau_{k,Y}^2}{(m_k+1)H^2}}\right], \tag{50}$$

from which we observe that χ_k'/κ_k depends on $\phi_{i,0}, e, \mathrm{B}_k$ and m_k, plus χ_k/κ_k. Now we have that $\chi_1/\kappa_1 = |A/\kappa_1| - \mathrm{B}_1/H$ and $\chi_2/\kappa_2 = |\varphi_\kappa A/\kappa_1 - \varphi_b| - \mathrm{B}_2/H$, and these depend also on the parameters of the base solution. Thus including α, we have reduced from 13 to 11 dimensionless parameters.

3.2 Dimensionless numbers

Our final stability problem remains formidable in terms of the 11-dimensional parameter space that we must consider. However, first we discuss the dimensionless parameters in relation to the dimensional physical parameters of the process. The reader is also referred to part 1, where much of this is explained. First of all, we consider a two-fluid flow through a narrow eccentric annulus of eccentricity e and angle of inclination β; $\phi_{i,0}$ has a similarly simple geometric interpretation.

The mean axial speed of the fluids (recall the flow rate is imposed) is denoted $\hat{w}^*$ and $\hat{\rho}^*$ denotes the maximum of the two fluid densities, (recall our convention of denoting dimensional quantities with the $\hat{}$ symbol). A shear rate scale $\hat{\dot{\gamma}}^*$ is defined by

$$\hat{\dot{\gamma}}^* = \frac{\hat{w}^*}{\hat{r}_o - \hat{r}_i},$$

where $\hat{r}_o$ and $\hat{r}_i$ are the outer and inner radii of the annulus, respectively. This is used to define a shear stress scale:

$$\hat{\tau}^* = \max_{k=1,2}\left\{\hat{\tau}_{k,Y} + \hat{\kappa}_k(\hat{\dot{\gamma}}^*)^{n_k}\right\},$$

and from this a viscosity scale $\hat{\mu}^* = \hat{\tau}^*/\hat{\dot{\gamma}}^*$. These are used to scale the dimensional rheological parameters: $\kappa_k = \hat{\kappa}_k(\hat{\dot{\gamma}}^*)^{n_k}/\hat{\tau}^*, \tau_{k,Y} = \hat{\tau}_{k,Y}/\hat{\tau}^*$, and hence we have that

$$\mathrm{B}_k = \frac{\hat{\tau}_{k,Y}}{\hat{\kappa}_k(\hat{\dot{\gamma}}^*)^{n_k}}.$$

The Bingham numbers thus denote the ratio of yield stress to purely viscous stress in each fluid. The power law indices, $n_k = 1/m_k$, describe the shear-thinning properties of the fluids; typically $n_k \leq 1$. The viscosity ratio $\varphi_\kappa = \kappa_1/\kappa_2$ is seen to be the ratio of purely viscous shear stresses in the two fluids. With respect to part 1, where we have considered only Newtonian fluids, the above definitions collapse to the Newtonian definitions in the case

that the yield stresses are zero ($B_k = 0$) and $n_k = 1$. Thus, essentially we have only four additional parameters to consider.

The two Reynolds numbers, Re_k, $k = 1, 2$, are the non-Newtonian counterparts of those defined in part 1:

$$\text{Re}_k = \frac{\hat{\rho}_k \hat{w}^* (\hat{r}_o - \hat{r}_i)^2}{\pi \hat{r}_a \hat{\kappa}_k (\hat{\dot{\gamma}}^*)^{n_k - 1}},$$

where $\hat{r}_a = 0.5(\hat{r}_o + \hat{r}_i)$ is the mean radius. These are *reduced* Reynolds numbers, relevant to the Hele-Shaw scaling, (i.e., the usual Reynolds number multiplied by the aspect ratio). Typically we would expect that $\text{Re}_k \lesssim 1$.

The buoyancy parameter φ_b is defined by:

$$\varphi_b = \frac{[\hat{\rho}_2 - \hat{\rho}_1] \hat{g} (\hat{r}_o - \hat{r}_i) \cos \beta}{\hat{w}^* \hat{\kappa}_2 (\hat{\dot{\gamma}}^*)^{n_2}},$$

which is a ratio between the axial buoyancy stresses and the viscous stresses in fluid 2. Use of the axial buoyancy stresses above results in the $\tan \beta$ term appearing in (49), which becomes singular for horizontal wells, $\beta = \pi/2$. Therefore, at times it will be convenient to work instead with

$$\varphi_b^* = \frac{[\hat{\rho}_2 - \hat{\rho}_1] \hat{g} (\hat{r}_o - \hat{r}_i)}{\hat{w}^* \hat{\kappa}_2 (\hat{\dot{\gamma}}^*)^{n_2}}.$$

Regarding the wavenumber α, note that the lengthscale used in the dimensionless model is $\pi \hat{r}_a$, and thus wavelengths of instabilities, $2\pi/\alpha$, need to be scaled appropriately. Using the eigenvalue λ will give an equivalent stability characterization to that using c, but time is measured in terms of the advective timescale, $\pi \hat{r}_a / \hat{w}^*$.

4 Simplified analyses

A number of simplified cases may be treated, for which analytical progress is possible.

4.1 Stability of single-fluid flows

First of all, let us suppose that we have the flow of a single fluid in the annulus. The stability problem is as above, but setting e.g. $\phi_{i,0} = 1$, suppressing the interface conditions, fluid 2 layer and subscripts. This leaves:

$$0 = D\left[\frac{\chi'(|\Psi_{0,\phi}|)}{\kappa} Df \right] - \alpha^2 \left[\frac{|A/\kappa|}{|\Psi_{0,\phi}|} \right] f, \quad -i\lambda\text{Re}\left(D(\frac{D}{H}) - \frac{\alpha^2}{H} \right) f, \qquad \phi \in (0, 1), \tag{51}$$

$$f(0) = 0, \tag{52}$$

$$f(1) = 0. \tag{53}$$

This eigenvalue problem shows some similarity to the Rayleigh equation, which admits continuous spectra for certain U (= base flow solution to the inviscid problem). Here, we note that the highest derivative, D^2 is multiplied by

$$\frac{\chi'(|\Psi_{0,\phi}|)}{\kappa} - \frac{i\lambda\text{Re}}{H}. \tag{54}$$

When (54) is zero, we expect there to be a continuous spectrum and possibly eigenfunctions that are singular at the azimuthal position where (54) is zero. On multiplying by the complex conjugate f^* and integrating over $[0, 1]$, we have

$$i\lambda\text{Re} = \frac{\displaystyle\int_0^1 \frac{\chi'(|\Psi_{0,\phi}|)}{\kappa} |Df|^2 + \alpha^2 \frac{|A/\kappa|}{|\Psi_{0,\phi}|} |f|^2 \, d\phi}{\displaystyle\int_0^1 \frac{|Df|^2 + \alpha^2 |f|^2}{H} \, d\phi}. \tag{55}$$

Thus, the single fluid flow has only imaginary eigenvalues with $\lambda_I < 0$, and is linearly stable.
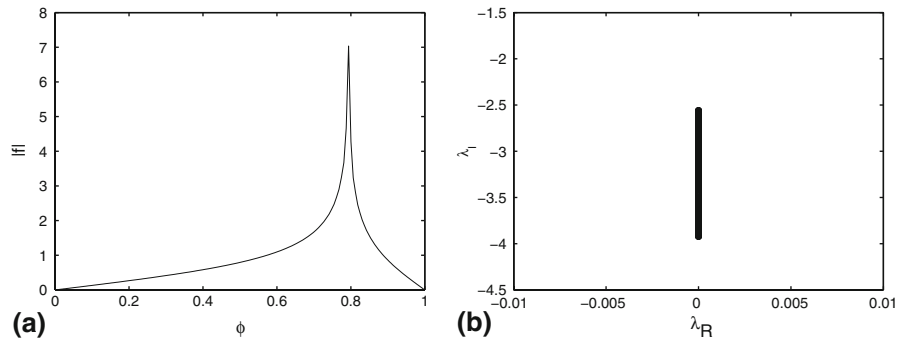
Fig. 5 Eigenfunction and spectrum for system (51)–(53): $\beta = 0$, $\kappa = 2.5$, $\rho = 1$, $m = 1$, $B = 2$, $\text{Re} = 1$, $e = 0.1$ and $\alpha = 0.1$. **a** Example eigenfunction. **b** Computed spectrum with $N = 201$

Figure 5 shows a typical eigenfunction and typical spectrum that can be computed numerically, (see later for description of the computational method). We use a spectral method, for which the (numerical) eigenfunctions are anyway smooth, but Fig. 5a is suggestive of a singular eigenfunction, as expected. The spectrum in Fig. 5b is computed with $N = 201$ numerical modes and we observe that the modes remain confined within a fixed interval. On increasing the number of numerical modes in the computation, we observe that the spectrum occupies the same fixed interval of the imaginary axis, but increasingly densely. The bounds of this interval on the imaginary axis can be deduced from the integral expression (55). When α is small the terms multiplying $|Df|^2$ dominate and we have:

$$-\max_{\phi}\left(\frac{\chi'(|\Psi_{0,\phi}|)H}{\kappa\text{Re}}\right) \leq \lambda_I \leq -\min_{\phi}\left(\frac{\chi'(|\Psi_{0,\phi}|)H}{\kappa\text{Re}}\right). \tag{56}$$

As we increase α we see that the terms multiplying $|f|^2$ come to dominate, leading to:

$$-\max_{\phi}\left(\frac{|A/\kappa|H}{|\Psi_{0,\phi}|\text{Re}}\right) \leq \lambda_I \leq -\min_{\phi}\left(\frac{|A/\kappa|H}{|\Psi_{0,\phi}|\text{Re}}\right). \tag{57}$$

For intermediate α we interpolate between the above bounds. Therefore we can bound λ_I for all α with

$$-\max\left\{\max_{\phi}\left(\frac{\chi'(|\Psi_{0,\phi}|)H}{\kappa\text{Re}}\right), \max_{\phi}\left(\frac{|A/\kappa|H}{|\Psi_{0,\phi}|\text{Re}}\right)\right\} \leq \lambda_I \leq -\min\left\{\min_{\phi}\left(\frac{\chi'(|\Psi_{0,\phi}|)H}{\kappa\text{Re}}\right), \min_{\phi}\left(\frac{|A/\kappa|H}{|\Psi_{0,\phi}|\text{Re}}\right)\right\}$$
$$\tag{58}$$

We illustrate the various bounds by the horizontal lines in Fig. 6. For increasing α it is observed that the spectrum shifts from (56) to (57).

4.2 Stability of 2-layer flows with static channels

In considering 2-fluid flows, in which one or both fluids have a static channel, we may also simplify things. First note that there are four different types of flow: (i) fluid 1 is fully static; (ii) fluid 1 is partly static; (iii) fluid 2 is fully static; (iv) fluid 2 is partly static. In addition there are combinations of these four possibilities.

Suppose that fluid k contains a static channel. If the entire fluid layer is static, then due to the eccentricity of the annulus this implies that the stress is below the yield stress by a finite amount everywhere in the layer (except perhaps at the widest part of the fluid layer, where it may be at exactly the yield stress). In this case, the infinitesimal linear perturbation cannot generate a finite stress perturbation and hence the velocity and stream-function perturbation is zero: $f_k = Df_k = 0$. According to the kinematic condition, either $h_0 = 0$ or $\lambda = 0$, implying neutral stability. However, with $h_0 = 0$, the interface is not perturbed and the stability problem in the other fluid layer becomes that of a single fluid, i.e., linearly stable by the method in Sect. 4.1 above. Therefore, the flows (i) and (iii) are linearly stable.
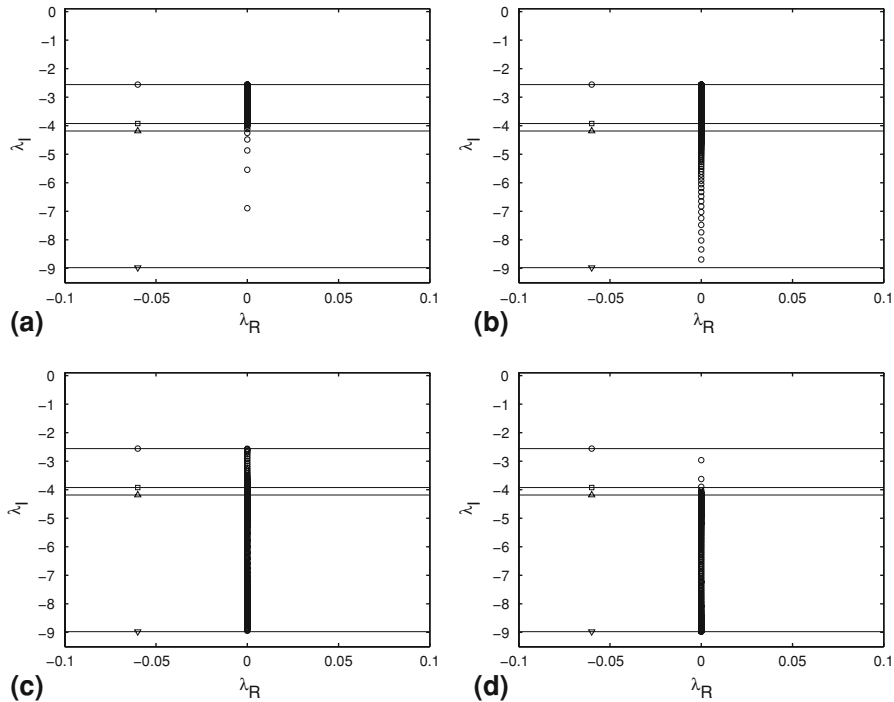
Fig. 6 Illustration of the bounds for λ_I: $\beta = 0$, $\kappa = 2.5$, $\rho = 1$, $m = 1$, $B = 2$, Re $= 1$ and $e = 0.1$. *Horizontal lines* marked with -o- and -△- correspond to the bounds (56), and those with -□- and -▽- correspond to the bounds (57). **a** $\alpha = 10$. **b** $\alpha = 100$. **c** $\alpha = 1000$. **d** $\alpha = 10000$

Let us consider (ii), where fluid 1 is partly static. Due to eccentricity, the mobile region is the wider part of the annulus so that we have mobile fluid 1 for $\phi \in [0, \phi_s)$ and static fluid for $\phi \in [\phi_s, \phi_i)$, for some ϕ_s. In considering perturbation of the solution and a possible perturbation to the yield surface, ϕ_s, after carefully linearising about ϕ_s we find that

$$Df_1(\phi_s) = \alpha f_1(\phi_s) = 0. \tag{59}$$

We now multiply (43) by f_1^* and integrate across $[0, \phi_s]$ in the manner of Sect. 4.1. This gives that either $f_1 = 0$ or $\lambda_I < 0$. Taking $f_1 = 0$, we may note that the interface is not perturbed. Therefore, $f_2(\phi_i) = 0$, we may multiply (44) by f_2^* and integrate across $[\phi_i, 1]$, to show that $f_2 = 0$ or $\lambda_I < 0$. This establishes that any flow of partially yielded fluid 1 will also be linearly stable. Physically, this occurs because the interface is static and cannot deform, which means that the stability problems in the yielded fluid layers are completely decoupled & treatable as single-fluid problems.

Finally consider situation (iv), where fluid 2 is partially yielded. Instability can only arise if fluid 1 is fully mobile in $[0, \phi_{i,0})$, and since the fluid layer is widest at $\phi = \phi_{i,0}$, fluid 2 is also mobile at the interface. The static fluid channel is now say $[\phi_s, 1]$. As before the static fluid channel is not perturbed, but now interfacial perturbations are possible. The full stability problem must be solved, but the domain for (44) is the mobile fluid layer: $\phi \in (\phi_{i,0}, \phi_s)$, and (46) is replaced by

$$Df_2(\phi_s) = \alpha f_2(\phi_s) = 0. \tag{60}$$

Note that an additional boundary condition is required to resolve the singular behaviour in (44) as $\phi \to \phi_s$.

4.3 Concentric annuli

For concentric annuli, $(H = 1)$, the base solution will have constant velocity in each fluid layer, so that (43) and (44) reduce to constant-coefficient equations. After long but straightforward manipulations, we find that either

$$\frac{\chi_k'}{\kappa_k} - \mathrm{i}\lambda \mathrm{Re}_k = 0, \quad k = 1, 2,$$

or λ satisfies:

$$0 = \mathrm{i}\alpha\varphi_b \tan\beta \sin\pi\phi_{i,0} + \varphi_\kappa \left[\frac{\chi_1'}{\kappa_1} - \mathrm{i}\lambda\mathrm{Re}_1\right] [\lambda - \alpha W_{i,1}] \, \nu_1 \coth \nu_1 \alpha\phi_{i,0}$$
$$+ \left[\frac{\chi_2'}{\kappa_2} - \mathrm{i}\lambda\mathrm{Re}_2\right] [\lambda - \alpha W_{i,2}] \, \nu_2 \coth \nu_2 \alpha(1 - \phi_{i,0}), \tag{61}$$

where

$$\nu_1 = \sqrt{\frac{\dfrac{|A/\kappa_1|}{|W_{i,1}|} - \mathrm{i}\lambda\mathrm{Re}_1}{\dfrac{\chi_1'}{\kappa_1} - \mathrm{i}\lambda\mathrm{Re}_1}}, \qquad \nu_2 = \sqrt{\frac{\dfrac{|\varphi_\kappa A/\kappa_1 - \varphi_b|}{|W_{i,2}|} - \mathrm{i}\lambda\mathrm{Re}_2}{\dfrac{\chi_2'}{\kappa_2} - \mathrm{i}\lambda\mathrm{Re}_2}},$$

and where the $W_{i,k}$ are the interfacial velocities of the base flow:

$$W_{i,k} = \frac{1}{H(\phi_{i,0})} \frac{\mathrm{d}}{\mathrm{d}\phi} \Psi_{k,0}(\phi_{i,0}), \quad k = 1, 2. \tag{62}$$

For a concentric annulus, $H = 1$ and these are also the constant velocities of each fluid layer.

Although we have been able to write down the above algebraic expression, it cannot be directly solved for λ, since λ appears also in ν_k. For the Newtonian fluids in part 1, the pressure-gradient flow-rate relation is linear, which leads to $\nu_k = 1$ and a quadratic equation for λ. Here the only practical use appears to be as a test condition for numerical solutions.

4.4 Long-wavelength analysis

The long-wavelength limit, $\alpha \to 0$, is studied by assuming a regular perturbation expansion in α for both λ and the solution to (43–49). After considerable algebra we find the following expressions:

$$\lambda \sim \alpha\lambda_1 + \alpha^2\lambda_2 + O(\alpha^3), \tag{63}$$
$$\lambda_1 = \frac{M_1 W_{i,2} + M_2 W_{i,1}}{M_1 + M_2}, \tag{64}$$
$$\lambda_2 = \mathrm{i} \left\{ -\frac{\varphi_b \tan\beta \sin\pi\phi_{i,0}}{3\pi\varphi_\kappa H(\phi_{i,0})} \left[\frac{M_1 M_2}{M_1 + M_2}\right] + \lambda_1 \frac{(W_{i,2} - W_{i,1})}{3} \left[\frac{\mathrm{Re}_1 N_1 M_2 - \mathrm{Re}_2 N_2 M_1}{(M_1 + M_2)^2}\right] \right\}, \tag{65}$$

where

$$M_1 = 3\pi \int_0^{\phi_{i,0}} \frac{\kappa_1}{\chi_1'(|\Psi_{1,0,\phi}|(\phi))} \mathrm{d}\phi,$$

$$M_2 = 3\pi\varphi_\kappa \int_{\phi_{i,0}}^1 \frac{\kappa_2}{\chi_2'(|\Psi_{2,0,\phi}|(\phi))} \mathrm{d}\phi,$$

$$N_1 = 9\pi \int\limits_0^{\phi_{i,0}} \frac{\kappa_1^2}{H(\phi)[\chi_1'(|\Psi_{1,0,\phi}|(\phi))]^2} \, \mathrm{d}\phi,$$

$$N_2 = 9\pi \varphi_\kappa \int\limits_{\phi_{i,0}}^1 \frac{\kappa_2^2}{H(\phi)[\chi_2'(|\Psi_{2,0,\phi}|(\phi))]^2} \, \mathrm{d}\phi.$$

These expressions reduce to those for two Newtonian fluids, (as given in part 1), in the limit $m_k = 1$ and $\mathrm{B}_k = 0$.

It is interesting to observe that the same structure persists for the non-Newtonian fluid combinations as for the Newtonian fluids. The first-order eigenvalue is advective (i.e., real), and propagates at a weighted average interfacial speed without growth or decay. The second-order eigenvalue is complex and controls the stability. As in part 1 we can see that $\rho_2 > \rho_1 \ (\Rightarrow b > 0)$ tends to stabilise the flow. Typically we will have $\lambda_1 > 0$ and then the second term in (65) is governed by the sign of:

$$(W_{i,2} - W_{i,1})(\mathrm{Re}_1 N_1 M_2 - \mathrm{Re}_2 N_2 M_1),$$

so that we can expect some form of checker-boarding when viewed in terms of interfacial velocity differences and Reynolds number differences.

5 Numerical results

For the remainder of the paper we consider parametric variations in the stability of the system of (43–49). Two tools are used for this. First, we solve numerically the full problem. Second, we consider the long-wavelength limit, $\alpha \to 0$. The long-wavelength limit gives sufficient conditions for linear instability, which is what we typically would like to predict. However, there are also some restrictions to the method, which we discuss and illustrate in Sect. 5.2.1.

The main part of our results we shall group in Sect. 5.2 and Sect. 5.3, exploring shear-thinning and yield-stress effects, respectively. Evidently, with an 11-dimensional parameter space to explore it is not possible to give a complete description of the stability. Our approach is to highlight the main qualitative features and illustrate this with concrete examples.

5.1 Numerical solution of the eigenvalue problem

The system (43–49) is solved using a spectral method. These are global methods that use the fully discretized stability operator, which is supplied to a matrix eigenvalue solver to give the spectrum. We have chosen a Chebyshev polynomial expansion to discretize our problem. The use of Chebyshev polynomials, especially in bounded domains, has proven very effective and accurate for such problems. The implementation of the method for our problem is fairly standard, as described in [15]. The boundary conditions are handled via the method described in Appendix III of [16], which generates spurious eigenvalues which are mapped to a fixed point in the complex plane, far outside of the domain of interest.

As in the Newtonian case, [15], the numerical spectra consist of two *interfacial* modes and two viscous spectra (each on the imaginary axis). The two interfacial modes can be identified with the kinematic condition (47) and the second jump condition at the interface, (49), both of which contain λ. These two modes are isolated.

In so far as the viscous spectra are concerned, they behave similarly to the spectra of the single-fluid problem, discussed in Sect. 4.1, in remaining bounded between limits and centered on the imaginary axis. However, we are uncertain whether the spectra are discrete or continuous in general. Do the jump conditions act to select only a countable number of combinations from the continuous spectra of the individual single fluid problems, posed on each fluid layer? Is this affected by whether or not the analogous limits to (58), derived for each individual fluid

layer, overlap one another? Do we have singular eigenfunctions in the viscous spectra? These are all interesting mathematical questions, but ones we have largely ignored from a theoretical standpoint. This is simply because the least stable mode is found to be either one of the interfacial modes, or otherwise is the least stable viscous mode (in which case the flow is anyway stable). This also explains why we have not used a very large number of modes, N, in our computations, i.e., increasing N adds further viscous modes but does not significantly change the position of the interfacial modes or the least stable viscous mode.

We note that the problem is different to some non-Newtonian stability problems, (i.e., certain visco-elastic fluids), where continuous spectra/singular eigenfunctions are found, due to the constitutive equations. Here the non-Newtonian effects simply manifest in (parametrically) different data functions within the linear equations and boundary conditions. The underlying mathematical problem is not qualitatively changed from the Newtonian problem. An exception to this might be thought to occur when we have a yield-stress fluid in the annulus. In this case χ'_k and $1/|\nabla\Psi|$ become singular at the yield surface. However, in the case that we have a yield surface, additional compatibility conditions are also satisfied by the stream function perturbation there, which render the perturbation equations regular. Details regarding this are given in [13]. A similar example of such problems is found in the study of shear instabilities for visco-plastic fluids, where the inclusion of a yield stress does not bring about continuous spectra; see e.g. [17].

As a test problem for our numerical method, we consider a concentric annulus. A typical computed spectrum for a concentric annulus is shown in Fig. 7a, for parameters $\beta = 0$, $\varphi_\kappa = 2.5$, $\varphi_b^* = -1$, $\phi_{i,0} = 0.5$, $e = 0.0$, $m_1 = 1$, $B_1 = 2$, $B_2 = 1$, $\mathrm{Re}_1 = 1$ and $\mathrm{Re}_2 = 0.5$. Note that numerically we have N polynomials for each fluid layer, leading to a $2N \times 2N$ linear system. Two of the numerical modes are spurious, used in each layer to impose the no-slip conditions, and 2 modes are isolated, corresponding to the interfacial modes. This leaves $N - 2$ viscous modes for each fluid. For the concentric annulus the viscous modes coalesce/collapse for each fluid into a single point, (with slight spreading of the spectra), which is given analytically by

$$\lambda = -\mathrm{i}\left(\frac{\chi'_k(|\Psi_{k,0,\phi}|)}{\kappa_k \mathrm{Re}_k}\right), \qquad k = 1, 2, \tag{66}$$

note this quantity is constant for each fluid in a concentric annulus. The interfacial modes are:

$\lambda_1 = 5.629131327699342 \times 10^{-2} + 1.339746353182102 \times 10^{-4}\mathrm{i}$

$\lambda_2 = -1.035574107944406 \times 10^{-2} - 4.351819831284716\mathrm{i}$.

To quantify the accuracy of our numerical method, we substitute in (61) to give squared residual values, denoted $|\lambda_e|^2$, $2.191933043525575 \times 10^{-7}$ and $2.191410609885782 \times 10^{-8}$, respectively. For the viscous modes we construct a residual error by subtracting the analytical values (66) and squaring. This gives maximal residual errors $|\lambda_e|^2 = 4.969136738725167 \times 10^{-16}$ and $|\lambda_e|^2 = 3.104767209945308 \times 10^{-20}$, for each fluid layer.

To better illustrate the collapse of the viscous spectra as $e \to 0$, Fig. 7b shows the spectrum for the same parameters as Fig. 7a but with a small eccentricity, $e = 0.1$. We observe that the viscous spectra have expanded into
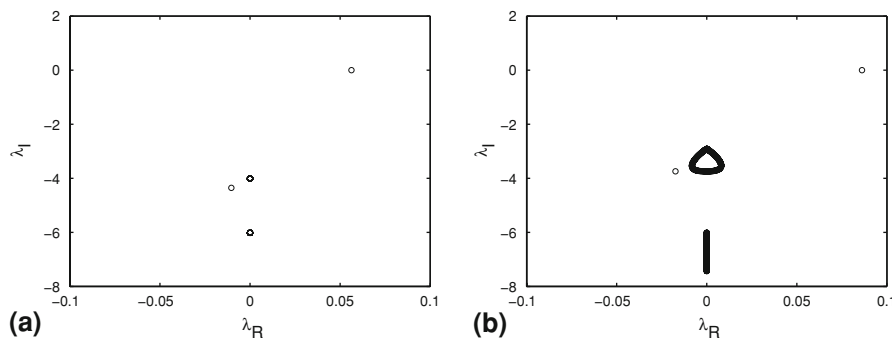

Fig. 7 Spectrum for system (43–49): $\beta = 0$, $\varphi_\kappa = 2.5$, $\varphi_b^* = 1$, $\phi_{i,0} = 0.5$, $m_1 = 1$, $B_1 = 2$, $B_2 = 1$, $\mathrm{Re}_1 = 1$ and $\mathrm{Re}_2 = 0.5$. **a** $e = 0.0$. **b** $e = 0.1$

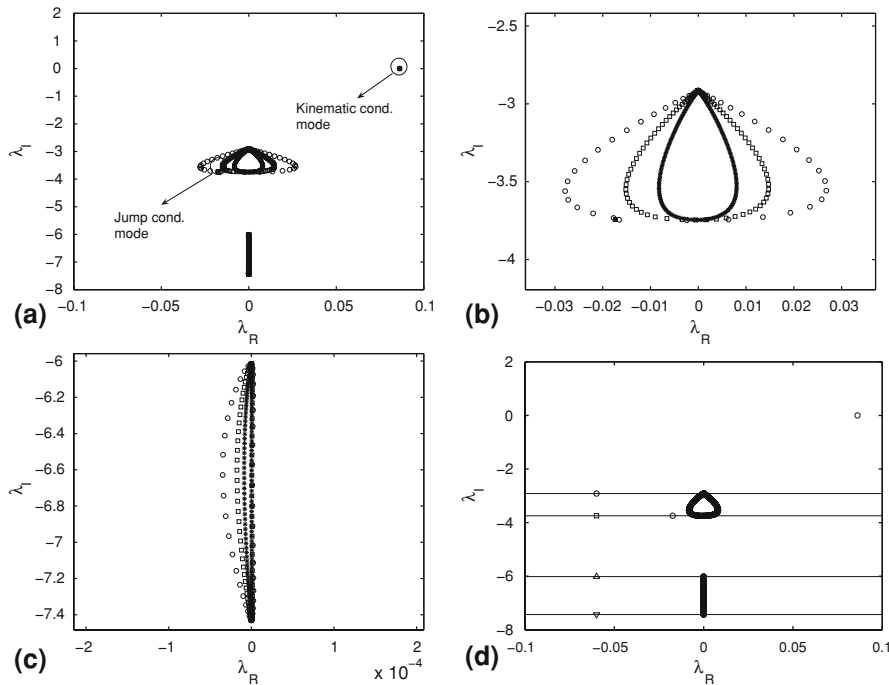**Fig. 8** Spectra for different numbers of nodes o-$N = 51$, □-$N = 100$ and *-$N = 200$. **a** Full spectra. **b** Zoom for viscous spectrum of fluid 1. **c** Zoom for viscous spectrum of fluid 2. **d** Bounds on λ_I for small α: -o- and -□- correspond to (67), -△- and -▽- correspond to (68). Parameters for all figures are $\beta = 0$, $\varphi_\kappa = 2.5$, $\varphi_b^* = 1$, $\phi_{i,0} = 0.5$, $m_1 = 1$, $B_1 = 2$, $B_2 = 1$, $\mathrm{Re}_1 = 1$, $\mathrm{Re}_2 = 0.5$, $e = 0.1$ and $\alpha = 0.1$

small loops, i.e., we do not have exactly $\lambda_R = 0$. This effect is purely numerical and is similar to what happens with the computed continuous spectrum of a Maxwell fluid, for example. As we increase the number of nodes this loop shrinks towards the imaginary axis line; see Fig. 8a–c. We are also able to derive estimates on the eigenvalues in the viscous spectra, analogous to those for the single fluid spectra:

$$- \max_{\phi \in [0, \phi_{i,0}]} \left(\frac{\chi_1'(|\Psi_{1,0,\phi}|) H}{\kappa_1 \mathrm{Re}_1} \right) \leq \lambda_I \leq - \min_{\phi \in [0, \phi_{i,0}]} \left(\frac{\chi_1'(|\Psi_{1,0,\phi}|) H}{\kappa_1 \mathrm{Re}_1} \right) \tag{67}$$

for fluid 1 and

$$- \max_{\phi \in [\phi_{i,0}, 1]} \left(\frac{\chi_2'(|\Psi_{2,0,\phi}|) H}{\kappa_2 \mathrm{Re}_2} \right) \leq \lambda_I \leq - \min_{\phi \in [\phi_{i,0}, 1]} \left(\frac{\chi_2'(|\Psi_{2,0,\phi}|) H}{\kappa_2 \mathrm{Re}_2} \right) \tag{68}$$

for fluid 2. In Fig. 8d we compare the viscous spectra for $\alpha = 0.1$ with these bounds. Note that in Fig. 8d, the bounds on fluid 1 are illustrated by the upper pair of horizontal lines, (this is purely due to the choice of parameters). On considering the full range of α we can also straightforwardly derive bounds analogous to (58) for each spectra.

Some examples eigenfunctions for the two-fluid problem are shown in Fig. 9, with the same parameters as Fig. 7b. Figure 9a shows the eigenfunction corresponding to the interfacial mode, which is regular. Figure 9b shows an eigenfunction corresponding to one of the viscous modes, which appears to be singular, suggestive of a continuous spectrum.

5.2 Shear-thinning effects

In order to explore parametric variations in some sort of systematic fashion, we utilise the long-wavelength approximation, which provides sufficient conditions for flow instability. We fix the interface position at mid-azimuth,
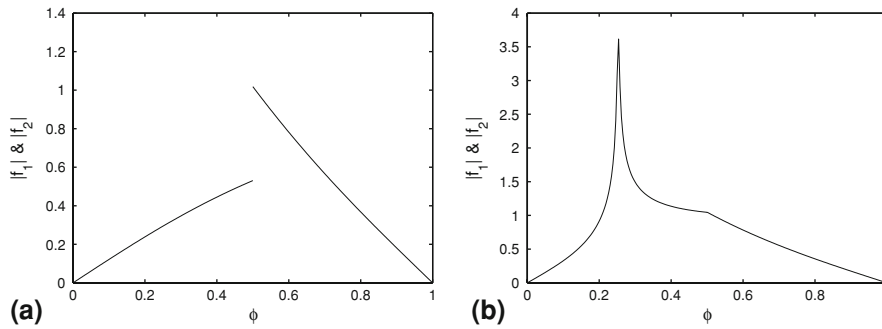
Fig. 9 Examples of eigenfunctions for system (43–49): $\beta = 0$, $\varphi_\kappa = 2.5$, $\varphi_b^* = 1$, $\phi_{i,0} = 0.5$, $m_1 = 1$, $B_1 = 2$, $B_2 = 1$, $\text{Re}_1 = 1$, $\text{Re}_2 = 0.5$, $e = 0.1$ and $\alpha = 0.1$. **a** Eigenfunction corresponding to kinematic mode. **b** Eigenfunction corresponding to a viscous mode for fluid 1
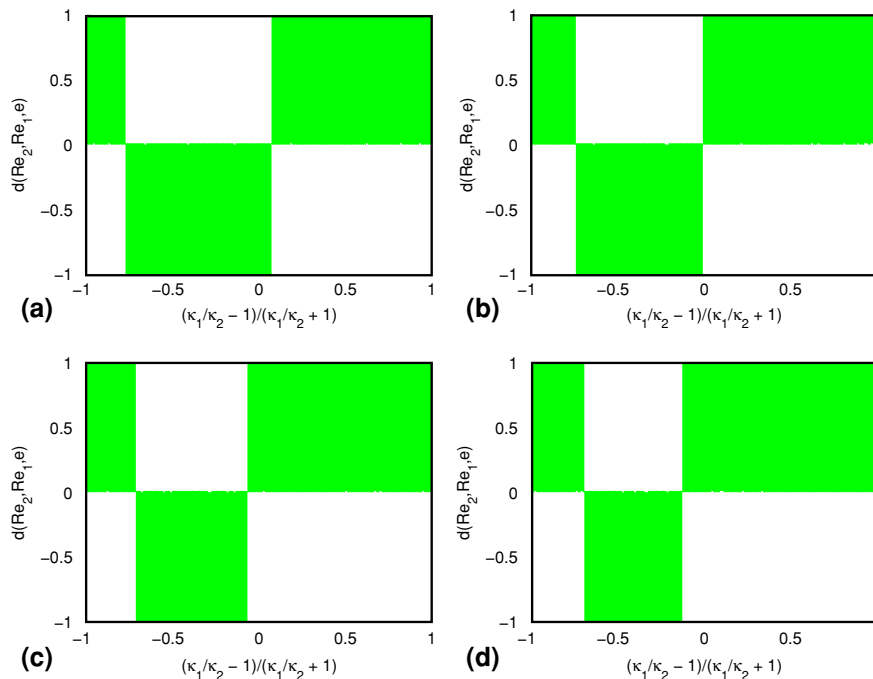

Fig. 10 Regions of marginal stability, long-wavelength approximation: $\beta = 0$, $\varphi_b^* = 1$, $\phi_{i,0} = 0.5$, $e = 0.1$, $m_1 = 1$, $B_1 = B_2 = 0$. **a** $m_2 = 4/3$. **b** $m_2 = 2$. **c** $m_2 = 3$. **d** $m_2 = 5$. Unstable *white*, stable *green* (*light grey*)

$\phi_{i,0} = 0.5$, and consider first vertical annuli $\beta = 0$. Figure 10 shows the effects of increasing m_2 at small eccentricity, i.e., we make the fluid that occupies the narrow side of the annulus progressively more shear-thinning. Figure 11 shows the same results but at a high eccentricity, $e = 0.5$.

We have plotted our results in the (x, y) plane where

$$x = \frac{\kappa_1/\kappa_2 - 1}{\kappa_1/\kappa_2 + 1}, \qquad y = d(\text{Re}_2, \text{Re}_1, e) = \frac{\text{Re}_2 N_2 M_1 - \text{Re}_1 N_1 M_2}{(M_1 + M_2)^2}.$$

Here x is simply a nonlinear mapping of the consistency ratio into $(-1, 1)$, whereas $d(\text{Re}_2, \text{Re}_1, e)$ enters directly into the stability criterion (65). The consistency ratio tends to affect the interfacial velocity difference, which also appears in (65). Indeed, for fixed well inclination the product $(W_{i,2} - W_{i,1})d(\text{Re}_2, \text{Re}_1, e)$ determines the long wave instability. Thus, the checkerboard of stable and unstable regimes in Figs. 10 and 11 is to be expected, as for $\beta = 0$
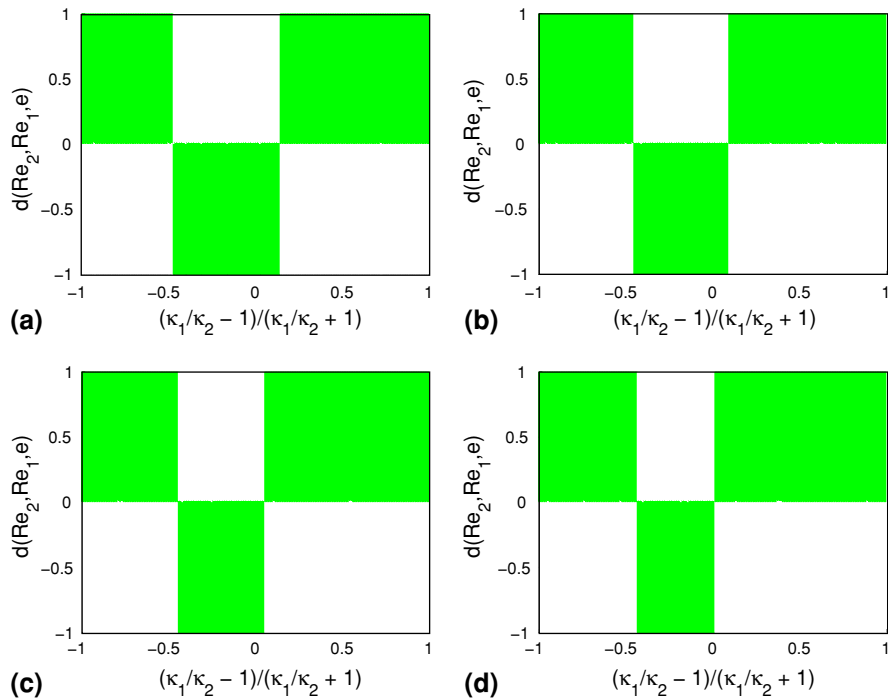
Fig. 11 As Fig. 10 with $e = 0.5$

buoyancy does not influence the long-wave instability (65). On the face of it, increased eccentricity does not result in a more or less stable flow, but simply a shifting in the checkerboard pattern.

We now look at horizontal wells, which represent the other directional extreme of the buoyancy force. For the same net buoyancy force, Figs. 12 and 13 show the analogous results to Figs. 10 and 11, but with $\beta = \pi/2$. Evidently, with a positive buoyancy gradient $\varphi_b^* = 1$, the horizontal flow is strongly stabilized. Figures 12 and 13 indicate that making the fluid on the narrow side of the annulus increasingly shear-thinning, (i.e., increasing m_2), apparently decreases the flow stability. Note that the parameters in the lower-right quadrant are physically difficult to achieve.

We have also computed a range of analogous results to Figs. 10–13 with m_2 fixed and varying m_1. The chequer-boarding patterns are similar qualitatively, but show quantitative differences. As with Figs. 10–13, the results are slightly ambiguous and do not give a clear indication of the effects of shear-thinning on stability.

5.2.1 Use of the long-wavelength approximation

Use of the long-wavelength approximation is clearly efficient computationally and the plots in Figs. 10–13 are probably the clearest way of presenting the long-wavelength stability. Although convenient and a valid indicator of instability, two problems with the long-wavelength analysis are: (i) the long-wavelength limit does not always predict the instability of the full problem, nor the maximal growth rates; (ii) the dimensionless variables that are convenient for the long-wavelength limit are not those useful for practical intuition. We illustrate both problems below, by solving the full stability system for example parameters.

We denote the least stable eigenvalue by $\lambda_{max} = \lambda_{R,max} + i\lambda_{I,max}$, i.e., that for which $\lambda = \lambda_R + i\lambda_I$ has maximal imaginary part. We now fix base parameters $\beta = 0$, $e = 0$, $\varphi_\kappa = 2.5$, $\varphi_b^* = 1$, $\phi_{i,0} = 0.5$, $B_1 = 0$, $B_2 = 0$, $Re_1 = 1$ and $Re_2 = 0.5$, (see Fig. 7a), and explore variation of the maximal eigenvalues with m_1 and m_2. In Fig. 14, we fix $m_2 = 1$ and take $m_1 = 4/3, 2, 3, 5$. At $m_1 = 1$ (Newtonian case) the flow is unstable and as we increase m_1 the flow remains unstable for all values of e. Physically, we are making fluid 1 thinner/less viscous, so perhaps this is physically intuitive. As the wavenumber α increases $\lambda_{I,max}$ changes smoothly until it asymptotes
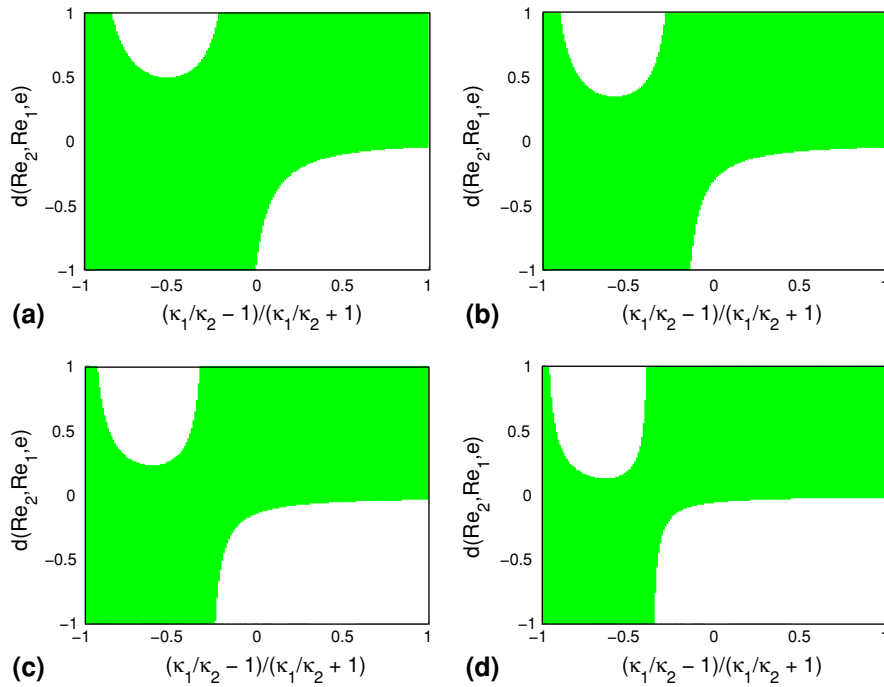
Fig. 12 As Fig. 10 with $\beta = \pi/2$

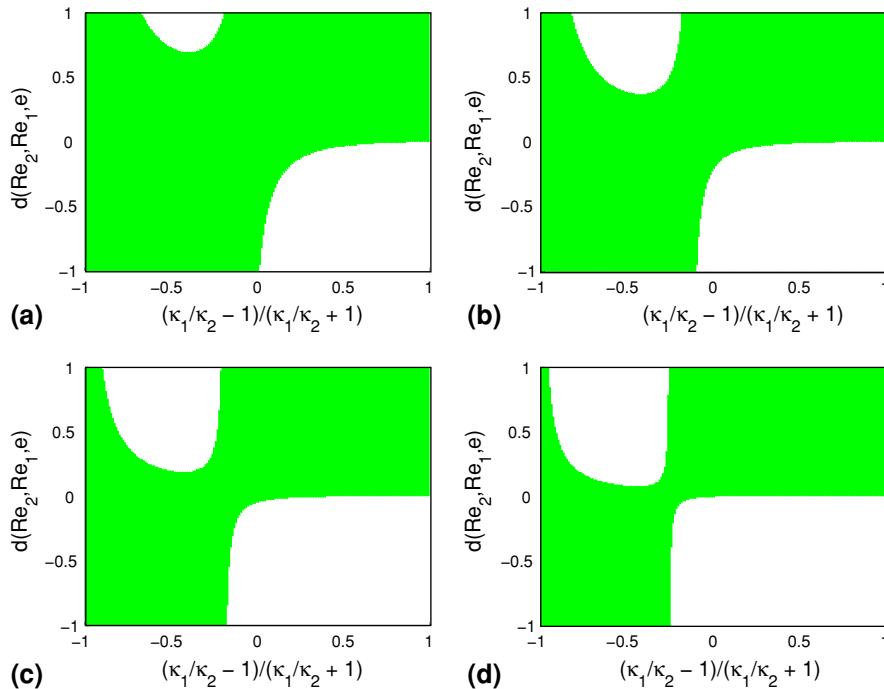**Fig. 13** As Fig. 11 with $\beta = \pi/2$

to the short-wavelength limit as $\alpha \to \infty$. Although the long-wavelength limit predicts the instability, the maximal growth rates are found in the short-wavelength limit or at some intermediate wavenumber, see Fig. 14c and d. In Fig. 15, we fix $m_1 = 1$ and consider changes in $m_2 = 4/3, 2, 3, 5$, for increasing e. A range of interesting
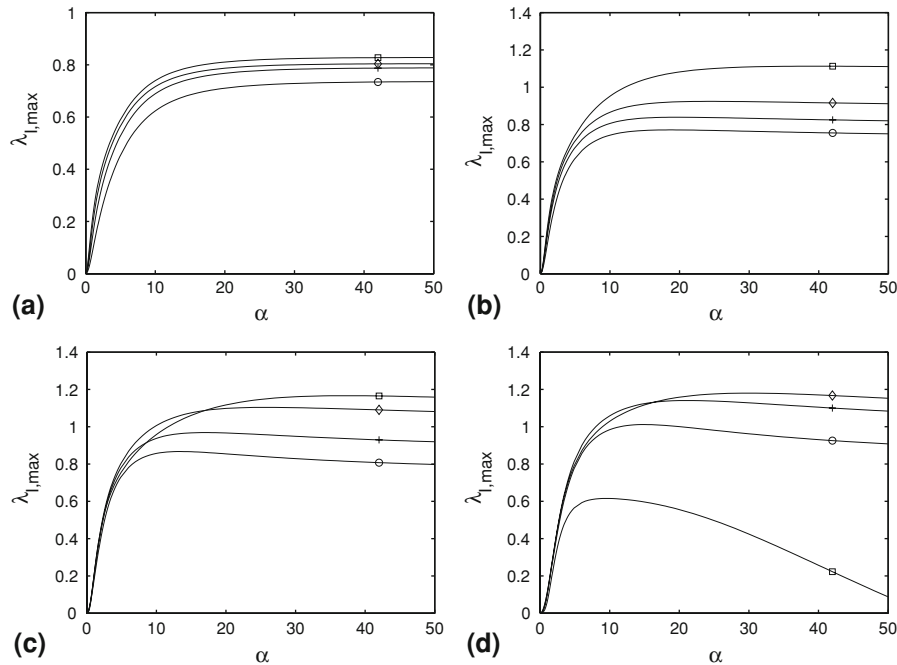
Fig. 14 Examples of typical variations in least stable eigenvalue with wavenumber: $\beta = 0$, $\phi_{i,0} = 0.5$, $\varphi_b^* = 1$, $Re_1 = 1$, $Re_2 = 0.5$, $\varphi_k = 2.5$, $B_1 = B_2 = 0$, $m_2 = 1$. **a** $e = 0.1$. **b** $e = 0.3$. **c** $e = 0.5$. **d** $e = 0.8$. In each figure $m_1 = 4/3$ (*marked with* ○), $m_1 = 2$ (*marked with* +), $m_1 = 3$ (*marked with* ◇), $m_1 = 5$ (*marked with* □)

behaviours are observed. First, the short-wavelength and long-wavelength limits clearly can give quite different stability predictions, as in Fig. 14. Second, we observe regions in which $\lambda_{I,max}$ is apparently constant. Thirdly, for small values of α, as we increase the power law index of fluid 2, we jump from an unstable flow to a stable flow; see e.g. $m_2 = 3$ and $m_2 = 5$.

The regions of near-constant $\lambda_{I,max}$ are explained in part 1, [15]. Essentially these regions are found when the interfacial modes become more stable than the least stable viscous mode. The least stable part of the viscous spectra is relatively insensitive to variations in α.

The jumping from stable to unstable at first appears strange, but is easily explained in the context of the long-wavelength approximation. Here, at fixed β, stability is governed by the product $(W_{i,2} - W_{i,1})d(Re_2, Re_1, e)$. As we increase any one rheological parameter both the interfacial velocities and $d(Re_2, Re_1, e)$ will change in a nonlinear fashion. It is this switching that leads to non-intuitive variations in stability. To illustrate this Fig. 16, plots $W_{i,2} - W_{i,1}$ and $d(Re_2, Re_1, e)$ for varying m_k, relative to the parameters in Figs. 14 and 15. In Fig. 16a and b we fix $m_2 = 1$ and vary m_1. We can see that $W_{i,2} - W_{i,1}$ and $d(Re_2, Re_1, e)$ have opposite sign and therefore the flow remains unstable. In Fig. 16c and d we fix $m_1 = 1$ and vary m_2. We can see that $W_{i,2} - W_{i,1}$ is always positive (fluid 2 is always less viscous) and $d(Re_2, Re_1, e)$ changes sign from negative to positive for increasing m_2, thus the flow will stabilize for large values of m_2. As we increase eccentricity the value of m_2 for which $d(Re_2, Re_1, e)$ changes sign increases. It is not possible to give a complete picture of even general rules regarding instability in the long-wavelength limit.

5.3 Yield-stress effects

We now consider yield-stress fluids, which are themselves shear-thinning. We can anticipate a similar level of complexity as for the power-law fluids in the above section. We therefore do not attempt to give a broad parametric study, but instead focus on those phenomena that are markedly different for yield-stress fluids. As discussed in
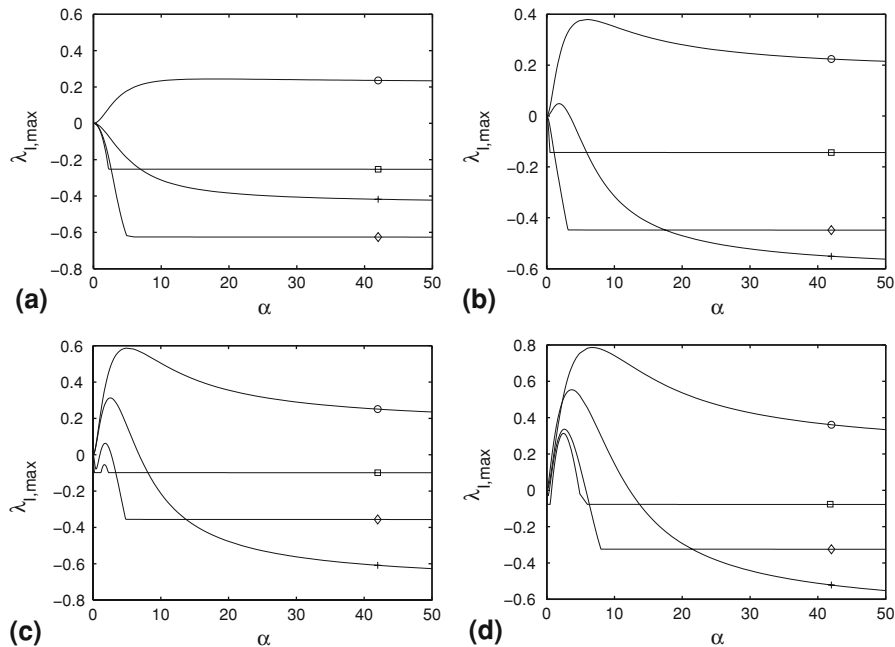
Fig. 15 Examples of typical variations in least stable eigenvalue with wavenumber: $\beta = 0$, $\phi_{i,0} = 0.5$, $\varphi_b^* = 1$, $Re_1 = 1$, $Re_2 = 0.5$, $\varphi_k = 2.5$, $B_1 = B_2 = 0$, $m_1 = 1$. **a** $e = 0.1$. **b** $e = 0.3$. **c** $e = 0.5$. **d** $e = 0.8$. In each figure $m_2 = 4/3$ (*marked with* ○), $m_2 = 2$ (*marked with* +), $m_2 = 3$ (*marked with* ◇), $m_2 = 5$ (*marked with* □)

Sect. 4.2, certain parameter combinations allow static channels to develop in the base flow and the majority of these flows are linearly stable. The occurrence of static channels is intuitively governed by the yield stresses of the fluids and width of the annular gap, i.e., by eccentricity and azimuthal position.

By way of illustration, below in Fig. 17 we show predictions of the long-wavelength theory (65), at different azimuthal positions in a vertical annulus with $e = 0.5$. Figure 18 shows analogous results in a horizontal annulus. What can be observed in Fig. 17 is that the usual checkerboard of stable and unstable regions is interrupted by large parameter regions where static channels are found in the base flow. Note that the base flow is independent of the Reynolds numbers. These same regions are found also in the horizontal annulus. Perhaps more interesting is that we see that there a direct transition from regions that are unstable, according to (65), to those with a static channel. This is a new type of transition and one that we should understand further.

Exploration of the spectrum of the full problem reveals that the addition of a yield stress appears to stabilise the flow by acting first on the short-wavelength limit. Thus, as the yield stress is increased instability is found eventually only in an increasingly small interval of wavenumbers close to $\alpha = 0$. An illustration of this is given in Fig. 19. Further increase of the fluid 1 yield stresses for the example in Fig. 19 results in the disappearance of the unstable interval and eventually the fluid 1 layer becomes static. This transition is characteristic of any of the transitions from stable to static regimes in Figs. 17–18.

A different transition occurs directly from unstable to static channel regimes. We illustrate this below in Fig. 20. For parameters: $\beta = 0$, $\varphi_b^* = 1$, $Re_1 = 1$, $Re_2 = 0.5$, $\varphi_k = 2.5$, $B_1 = 0.1$, $B_2 = 1$, $m_1 = m_2 = 1$, $\phi_{i,0} = 0.8$, we approach the static channel regime by progressively increasing the eccentricity, e. We present the evolution of the least stable eigenvalues of system (43–49) for $e \in [0.3, 0.9]$ in Fig. 20a. The viscous spectrum remains fairly fixed, stabilising slightly. The main change is observed in the interfacial mode. As the static channel is approached, $\lambda_{I,max} \to 0$ from above, but also $\lambda_{R,max} \to 0$. We have presented only results for $\alpha = 1$, although other wavenumbers are similar. Figure 20b shows the base velocity solution for $e = 0.3$ and $e = 0.9$. For $e = 0.9$ the fluid 2 layer is nearly static, with $|\Psi_{2,0,\phi}| \sim 10^{-6}$.
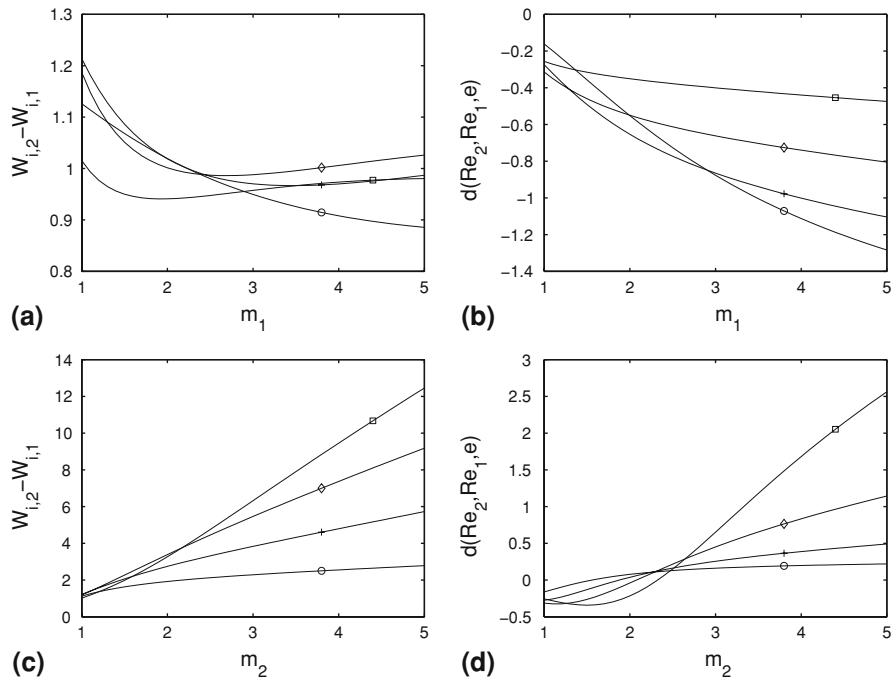
Fig. 16 Examples of typical variations for $W_{i,2} - W_{i,1}$ and $d(\mathrm{Re}_2, \mathrm{Re}_1, e)$ for varying m_k: $\beta = 0$, $\phi_{i,0} = 0.5$, $\varphi_b^* = 1$, $\mathrm{Re}_1 = 1$, $\mathrm{Re}_2 = 0.5$, $\varphi_k = 2.5$, $B_1 = B_2 = 0$. **a, b** $m_2 = 1$. **c, d** $m_1 = 1$. In each figure $e = 0.1$ (*marked with* $\circ$), $e = 0.3$ (*marked with* $+$), $e = 0.5$ (*marked with* $\diamond$), $e = 0.8$ (*marked with* $\square$)
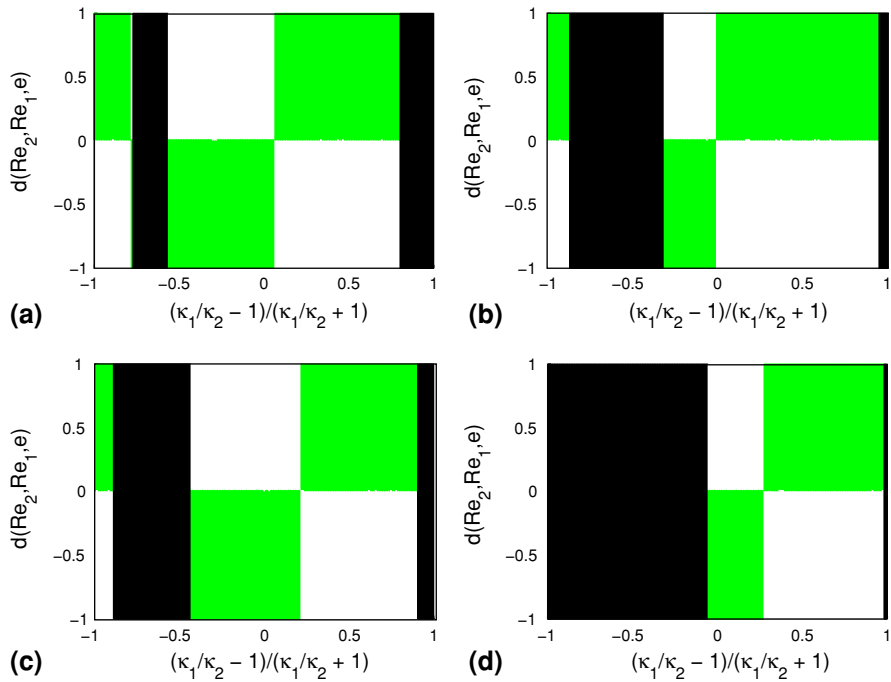

Fig. 17 Regions of marginal stability, long-wavelength approximation: $\beta = 0$, $\varphi_b^* = 1$, $e = 0.5$, $m_1 = m_2 = 1$: **a** $\phi_{i,0} = 0.25$, $B_1 = 1$, $B_2 = 0.5$. **b** $\phi_{i,0} = 0.75$, $B_1 = 1$, $B_2 = 0.5$. **c** $\phi_{i,0} = 0.25$, $B_1 = 0.5$, $B_2 = 1$. **d** $\phi_{i,0} = 0.75$, $B_1 = 0.5$, $B_2 = 1$. Unstable (*white*), stable (*green (light grey)*), unyielded/static channel (*black*)
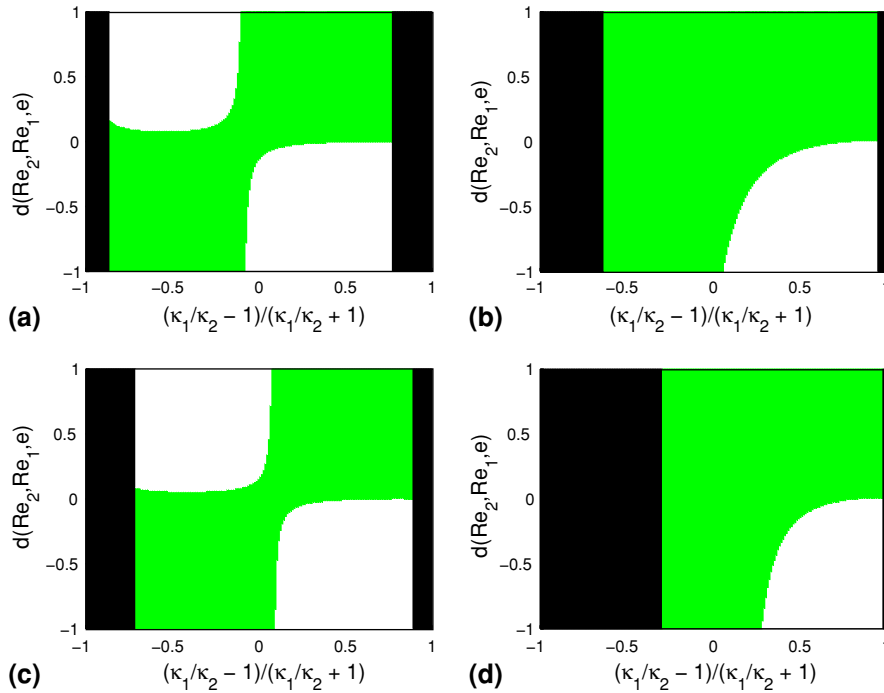
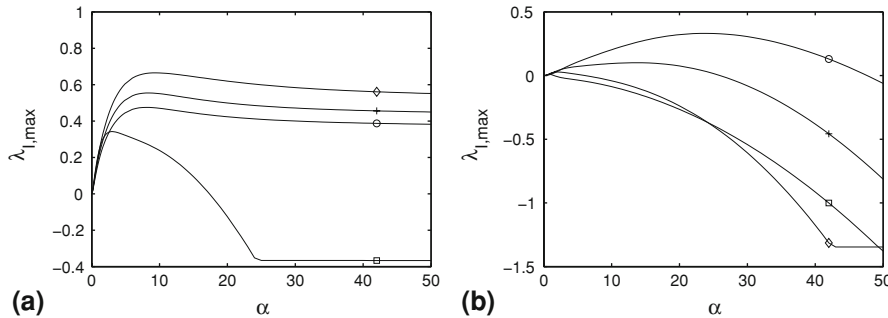**Fig. 18** As Fig. 17 with $\beta = \pi/2$

Fig. 19 Examples of typical variations in least stable eigenvalue with wavenumber: $e = 0.5$, $\beta = 0$, $\varphi_b^* = 1$, $Re_1 = 1$, $Re_2 = 0.5$, $\varphi_k = 2.5$, $B_2 = 0.5$, $m_1 = m_2 = 1$. **a** $\phi_{i,0} = 0.25$. **b** $\phi_{i,0} = 0.75$. In each figure $B_1 = 0.1$ (*marked with* ○), $B_1 = 0.5$ (*marked with* +), $B_1 = 1$ (*marked with* ◇), $B_1 = 2$ (*marked with* □)

The approach to the static layer flow is easier to understand via analysis of the long-wavelength limit (65). From the results in [9] we know that $\chi_k(|\nabla\Psi|) \sim |\nabla\Psi|^{n_k/(n_k+1)}$ as $|\nabla\Psi| \to 0$. Thus, $\chi_k'(|\nabla\Psi|) \sim |\nabla\Psi|^{-1/(n_k+1)}$ as $|\nabla\Psi| \to 0$. This singular behaviour causes difficulties for numerical solution of (43–49), and some numerical noise can be observed in the calculated $\lambda_{I,max}$ in Fig. 20a, as e becomes large. From (65) and the asymptotic behaviour of χ_k' we can resolve the leading-order behaviour of λ at $\alpha = 0$ as the static channel is approached:

$$\lambda_1 \sim O(|\Psi_{2,0,\phi}|^{1/(n_2+1)}),$$

$$\lambda_2 \sim O(\varphi_b^* \sin\beta |\Psi_{2,0,\phi}|^{1/(n_2+1)}) + O(|\Psi_{2,0,\phi}|^{2/(n_2+1)}).$$

The signs of the constants in the above limiting expression will be governed by the fluid 1 velocity profile, which remains $O(1)$ and in fact changes very little as fluid 2 becomes progressively static. Thus, the slightly strange transition direct from instability to the static channel is explained.
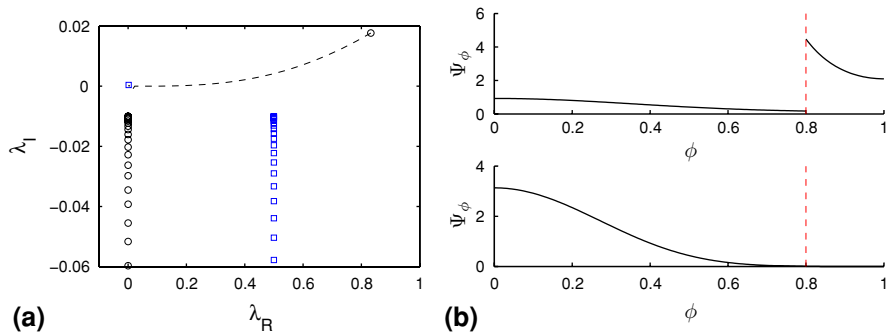
Fig. 20 Transition from unstable to static channel for parameters: $\beta = 0$, $\varphi_b^* = 1$, $Re_1 = 1$, $Re_2 = 0.5$, $\varphi_k = 2.5$, $B_1 = 0.1$, $B_2 = 1$, $m_1 = m_2 = 1$, $\phi_{i,0} = 0.8$, with increasing eccentricity e. Figure (**a**) shows the evolution of the least stable (interfacial) mode as e is varied from $e = 0.3$ (*marked with* ○) to $e = 0.9$ (*marked with* □); see *broken line*. We also show the viscous spectrum at $e = 0.3$ and $e = 0.9$; that at $e = 0.9$ (*marked with* □) is offset along the real axis by 0.5 for clarity. Figure (**b**) shows the base solution at $e = 0.3$ and $e = 0.9$

6 Discussion

We have considered a practically relevant generalisation of [15] to the case of shear-thinning and yield-stress fluids, as are commonly used in primary cementing. Although the methodology is similar to the Newtonian case, there are a number of interesting differences in the results.

The occurrence of static mud channels in primary cementing has been known of since the 1960s, [4] and is a major cause of process failure. We have seen here that static channels can occur in either fluid layer, in the displaced or displacing fluid. It is those that occur on the narrow side of the annulus that are of most direct industrial relevance. Here we have quantified this phenomenon via the maximal volume fraction of residual fluid that is possible to be left behind in the annulus, f_{static}. We have shown that f_{static} depends on five dimensionless parameters and have presented a range of results that illustrate this dependency. In general f_{static} is quick to compute as the solution of a simple nonlinear equation.

Via dimensional analysis, we have shown that the base solutions depend on a minimal set of eight dimensionless parameters, which is four more than the Newtonian fluid case in part 1. These additional parameters are the two power-law indices and two Bingham numbers. These additional parameters thus capture the shear-thinning and yield-stress effects. The stability problem depends on an additional three dimensionless parameters: two Reynolds numbers and a wavenumber.

A range of analytical and semi-analytical results have been derived. For the industrially problematic static channel flows, we show that three of the four different types of static channel flows are linearly stable. The fourth type of static channel flow may be stable or unstable, this involves simply a restriction of the yielded channel width, but the interface has yielded fluid on both sides.

The most useful semi-analytical results certainly come from the long-wavelength analysis. Here we have provided an equivalent characterisation of the stability to that in [15] for the Newtonian fluids. By this we mean that the final formulae for the eigenvalue contain equivalent terms to those in [15], albeit modified in a nonlinear fashion to account for the fluids. The formulae may be simply evaluated once the base flow is calculated and hence are suitable for rapid computation, e.g. as part of a process optimisation. In a similar way to the Newtonian fluid case, in the absence of buoyancy instability is governed by a product between the difference in interfacial velocities and a weighted difference in Reynolds number for the two fluids. The switching of signs of the terms in this product is responsible for much of the complexity that we observe in the results. When density differences are included the stability is changed in a fairly predictable way.

For power-law fluids, i.e., only with shear-thinning effects, for vertical annuli we can make no simple statements regarding stability. For horizontal annuli with $\varphi_b > 0$ the flow is stabilised. As the fluids become more shear-thinning the stability is slightly reduced.

Addition of a yield stress has the general effect of suppressing short-wavelength instabilities. We also have the phenomenon of static channels, described above, which are commonly stable. Thus, our parametric results exhibit an additional two types of transition, from stable to static channel and direct from unstable to static channel. The latter is, of course, quite surprising and we have investigated the transition in detail, showing that the growth rates can indeed approach zero from above as the fluid channel "solidifies".

In terms of practical matters, the most relevant fact is that static channels with an unyielded interface are linearly stable. This tends to suggest that ideas related to flow pulsation and the instigation of instability may not destabilise the mud channels. In short, the formation of static mud channels needs to be avoided as once formed they are likely to persist.

An area that we have not touched here is which base parameters are likely to lead to multi-layer flows of the type studied here. Multi-layer flows only arise from an ineffective underlying displacement for which the interface elongates into a pseudo-parallel flow; see Fig. 1f. Many parameter regimes lead to displacements that are in fact effective, i.e., steady traveling waves; see [8–10]. The analysis in [7] provides one method for predicting whether displacements will be steady or unsteady. Ideally, for practical application of the results in this paper we need to couple the predictions of a model such as in [7], with those from our work here, i.e., there is no point to consider the stability of a flow that never evolves in the first place.

References

1. Economides MJ (1990) Implications of cementing on well performance. In: Nelson EB (ed) Well cementing. Schlumberger Educational Services, Houston
2. Primary and Remedial Cementing Guidelines. Drilling and Completions Committee, Alberta, April 1995. Distributed by the Petroleum Industry Training Service
3. Nelson EB (ed) (2001) Well cementing. Schlumberger Educational Services, Houston
4. McLean RH, Manry CW, Whitaker WW (1966) Displacement mechanics in primary cementing. Society of Petroleum Engineers paper number SPE 1488
5. Guillot D, Hendriks H, Callet F, Vidick B (1990) Mud removal. In: Nelson EB (ed). Well cementing. Schlumberger Educational Services, Houston
6. Lockyear CF, Ryan DF, Gunningham MM (1989) Cement channelling: how to predict and Prevent. Society of Petroleum Engineers paper number SPE 19865
7. Pelipenko S, Frigaard IA (2004) Visco-plastic fluid displacements in near-vertical narrow eccentric annuli: prediction of travelling wave solutions and interfacial instability. J Fluid Mech 520:343–377
8. Bittleston SH, Ferguson J, Frigaard IA (2002) Mud removal and cement placement during primary cementing of an oil well; laminar non-Newtonian displacements in an eccentric annular Hele-Shaw cell. J Eng Math 43:229–253
9. Pelipenko S, Frigaard IA (2004) On steady state displacements in primary cementing of an oil well. J Eng Math 46(1):1–26
10. Pelipenko S, Frigaard IA (2004) Two-dimensional computational simulation of eccentric annular cementing displacements. IMA J Appl Math 64(6):557–583
11. Tehrani A, Ferguson J, Bittleston SH (1992) Laminar displacement in annuli: a combined experimental and theoretical study. Society of Petroleum Engineers paper number SPE 24569
12. Tehrani A, Bittleston SH, Long PJG (1993) Flow instabilities during annular displacement of one non-Newtonian fluid by another. Exp Fluids 14:246–256
13. Moyers-González MA (2006) Transient effects in oilfield cementing flows. Ph.D. dissertation, University of British Columbia
14. Moyers-González MA, Frigaard IA, Scherzer O, Tsai TP (2007) Transient effects in oilfield cementing flows: qualitative behaviour. Euro J Appl Math 18:477–512
15. Moyers-González MA, Frigaard IA (2007) Kinematic instabilities in two-layer eccentric annular flows, part 1: Newtonian fluids. J Eng Math doi:10.1007/s10665-007-9178-y
16. Schmid PJ, Henningson DS (2001) Stability and transition in shear flows. Springer-Verlag, New York
17. Frigaard IA, Howison SD, Sobey IJ (1994) On the stability of Poiseuille flow of a Bingham Fluid. J Fluid Mech 263:133–150